

This item is	the a	archived	peer-reviewed	author-	version •	of:

Increasing the phase stability of CsPbl₃ nanocrystals by Zn2+ and Cd2+ addition : synergy of transmission electron microscopy and molecular dynamics

Reference:

Skvortsova Irina, Braeckevelt Tom, de Backer Annick, Schrenker Nadine, Pradhan Bapi, Hofkens Johan, Van Aert Sandra, Van Speybroeck Veronique, Bals Sara.- Increasing the phase stability of CsPbl₃ nanocrystals by Zn2+ and Cd2+ addition: synergy of transmission electron microscopy and molecular dynamics ACS nano - ISSN 1936-0851 - 19:18(2025), p. 17698-17708
Full text (Publisher's DOI): https://doi.org/10.1021/ACSNANO.5C01825

To cite this reference: https://hdl.handle.net/10067/2141070151162165141

uantwerpen.be

Increasing the phase stability of CsPbI₃ nanocrystals by Zn²⁺ and Cd²⁺ addition: synergy of transmission electron microscopy and molecular dynamics

Irina Skvortsova¹‡, Tom Braeckevelt^{2,3}‡, Annick De Backer¹, Nadine Schrenker¹, Bapi Pradhan³, Johan Hofkens³, Sandra Van Aert¹, Veronique Van Speybroeck², Sara Bals^{1*}

¹ Electron microscopy for materials science (EMAT) and NANOlab Center of Excellence, University of Antwerp, Groenenborgerlaan 171, 2020 Antwerp, Belgium

² Center for molecular modeling (CMM), Ghent University, Technologiepark 46, 9052 Zwijnaarde, Belgium

³ Department of Chemistry, KU Leuven, Celestijnenlaan 200F, 3001 Leuven, Belgium

‡These authors contribute equally

*Corresponding author: sara.bals@uantwerpen.be

ABSTRACT: Metal halide perovskites (MHPs) are emerging as promising materials for optoelectronic and photovoltaic applications due to their favorable electronic properties, including a tunable bandgap. However, achieving high stability for these materials remains a critical challenge, particularly for CsPbI₃, whose photoactive phases spontaneously convert into a non-

photoactive yellow orthorhombic δ-phase under ambient conditions. This transformation results in a significant increase in bandgap and a loss of photoactive functionality. In this study, we investigate the impact of Zn²⁺ and Cd²⁺ dopants on the phase stability of CsPbI₃ nanocrystals (NCs), emphasizing the formation of Ruddlesden-Popper (RP) planar defects, which are frequently observed during compositional tuning. Using transmission electron microscopy (TEM), we follow the temporal evolution of the phase transformation, where black-phase NCs agglomerate and form elongated microtubes with yellow-phase crystal structure. Our observations demonstrate that doped samples are significantly more stable, while the dopants are key factors in the formation of the RP-like defects with specific atomic arrangements. Using a combination of quantitative TEM and molecular dynamics (MD) simulations we characterize the structure and composition of asfound RP-like defects and elucidate their role in stabilizing the photoactive phases of CsPbI₃ through decreased phase transition kinetics.

KEYWORDS: perovskites, doping, Ruddlesden-Popper phase defects, phase stability, transmission electron microscopy, molecular dynamics

INTRODUCTION:

Metal halide perovskites with the general formula ABX₃ are promising candidates for the next generation of optoelectronic and photovoltaic devices¹. This class of materials yields a crystal structure, where eight corner-sharing $[BX_6]^{4-}$ octahedra form a three-dimensional network with an A-cation in the center. The electronic properties of these materials are mainly determined by the coordination environment of B-metal cations and by the hybridization between the orbitals of B-metal cations and X halide anions². The photoactive (cubic (α) /tetragonal (β) or orthorhombic (γ))

CsPbI₃ structures (Figure S1 (a)) yield a bandgap of 1.6-1.8 eV³, which is favorable for solar cell applications^{4,5,6,7} and makes this material a perfect candidate for red light emitting diodes (LED)^{8,9}. A major obstacle to realize CsPbI₃-based devices is that the photoactive, also called 'black', phases are not thermodynamically stable at ambient conditions and spontaneously convert into a 'yellow' non-photoactive orthorhombic δ -phase (Figure S1(b))^{10,11}. The phase transition energy barriers are low in air due to the presence of H₂O molecules/OH⁻ dissociation species^{12,13,14,15} which are adsorbed onto the CsPbI₃ surface and partially dissolve halide anions, creating vacancy defect sites, thus making these transitions more favorable¹⁶. At the same time, other types of metal halides exhibit different degradation pathways depending on their composition and crystal structure¹⁷.

The yellow phase has a distorted perovskite structure with a low degree of hybridization arising from different, compared to the black phase, cation and anion orderings, where $[PbI_6]^{4-}$ octahedra share their edges instead of corners (Figure S1(a, b)). This results in a higher band gap of 2.83 eV¹¹, which makes δ -CsPbI₃ significantly less efficient in utilization for energy conversion. Previous studies suggest that strategies such as strain engineering^{18,19}, surface coating²⁰, ligand modification²¹ and compositional tuning^{22,23} could substantially improve the phase stability of CsPbI₃ NCs. Compositional tuning is frequently associated with the formation of Ruddlesden-Popper (RP) planar defects, as shown in the literature for CsPbBr₃ doped with transition metals^{24,25} and for CsPbX₃ with mixed halide composition²⁶. The RP phase (Figure S1(c)) has the general formula Cs_{n+1}Pb_nX_{3n+1} and consists of n perovskite layers separated by a CsX layer, where n is an integer. Remarkably, the underlying reasons for the formation of RP phases, and their effect on phase stability are not yet fully understood.

Here, we performed a combined experimental-computational study to unravel the effect of adding Zn²⁺ and Cd²⁺ precursors on the phase stability of CsPbI₃ NCs and their connection with

the formation of RP phases. TEM was used to investigate the morphology, structure and composition of the beam-sensitive²⁷ perovskite NCs at a local scale. In this manner, we were able to characterize specific types of RP-like defects found across the doped NCs. By combining these experimental results with molecular dynamics (MD) simulations based on Machine Learning Potentials, we could reveal how and why the RP planar faults are formed in the presence of Zn²⁺ and Cd²⁺. Moreover, we were able to understand the role of these two types of planar defects in phase stabilization. As such, our study enables an enhanced understanding of the mechanisms underlying perovskite stabilization, which can trigger the synthesis of more stable metal halide perovskite NCs that can be exploited in a variety of optoelectronic applications.

RESULTS AND DISCUSSION:

Phase stability of undoped, Zn- and Cd-doped CsPbI3 NCs by ex situ TEM imaging

CsPbI₃ NCs, doped by Zn and Cd, were obtained through optimized versions of previously reported synthesis approaches^{23,28}. Cd and Zn have significantly different ionic radii (Cd²⁺ in tetrahedral coordination: 0.78 Å; Cd²⁺ in octahedral coordination: 0.95 Å and Zn²⁺ in tetrahedral coordination: 0.6 Å; Zn²⁺ in octahedral coordination: 0.74 Å) in comparison to Pb (Pb²⁺ in octahedral coordination: 1.19 Å)^{29,30}. This difference is expected to impact the perovskite structure and, consequently, its phase stability.

Three samples were further analyzed: undoped CsPbI₃ NCs, CsPbI₃ NCs doped with Cd and CsPbI₃ NCs doped with Zn. Unfortunately, metal halide perovskites are sensitive to the electron beam during investigations by transmission electron microscopy (TEM). We therefore applied high-angle annular dark-field scanning transmission electron microscopy (HAADF-STEM) imaging with the total dose up to 1500 e⁻/Å², to avoid electron beam-induced radiolysis^{31,32}

typically resulting in metallic Pb/PbX₂ cluster formation and halide desorption. Pristine and doped CsPbI₃ NCs with cube-like shape (Figure S2 (a, b, c)) were found in the 'black' γ-orthorhombic (*Pnma*, No. 62) crystal structure (Figure S2 (d, e, f)). All samples were investigated by energy dispersive X-ray spectroscopy (EDX), which confirmed the presence of ~2.1 at.% of Zn and ~2.5 at.% of Cd (Figure S3, Table S1).

To investigate the stability of these samples, we exposed three different TEM grids with NCs (pristine, Cd and Zn doped) to air (with relative humidity of ~40%) at 20 °C, while performing TEM investigations after different time intervals (6, 12 hours, 1 day, 5 days, 10 days). These observations (Figure 1 (a, d, e)) show that all samples degraded, but the pristine sample was significantly less stable in comparison to the doped samples. For all materials, structural degradation of the NCs under ambient conditions occurred in two stages. In the first stage, agglomeration was observed (white circles in Figure 1 (a)), which was accompanied by a shape transformation of the NCs and grain boundaries formation between them (Figure 1 (b), white **arrow**). Eventually, this process resulted in the formation of the microtubes. Interestingly, the perovskite orthorhombic structure (Pnma) was preserved in this first stage of the degradation process (Figure 1(b)). In the second degradation stage, a structural transformation into the nonperovskite (yellow) phase has occurred (Figure 1(b)). The undoped material went through agglomeration and phase transition within only 24 hours, resulting in yellow phase hollow microtubes and nanowires with their long axis oriented along the (100) plane and with a length of 2-8 µm. Control experiments showed that structural degradation of the NCs on a TEM grid proceeds within a similar period as NCs kept in solution (Figure 1 (c)) under the open air and the solution color changes from red to orange and eventually to yellow. The timescale of the undoped CsPbI₃ degradation furthermore matches with previously reported X-ray diffraction data²². For the

doped samples, these morphologies were observed after 5 days and 10 days for Cd- and Zn-doped samples, respectively (**Figure 1 (d, e)**). The elongated morphology appeared to be favorable for the yellow phase matching with previously reported study^{33,34}.

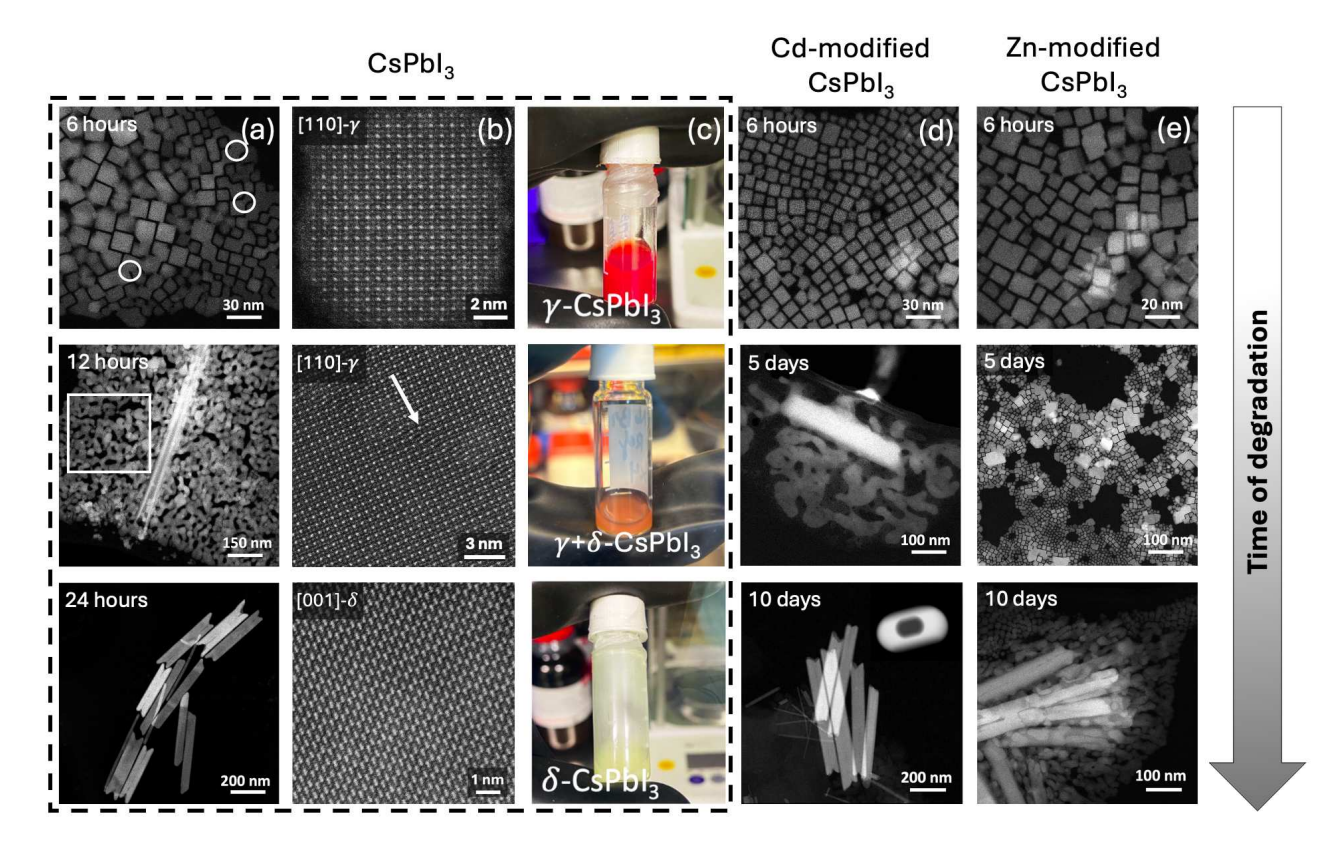


Figure 1. HAADF-STEM overview (a) and high-resolution images (b) of undoped CsPbI₃ recorded upon degradation during 6, 12, 24 hours in air with the corresponding color changes (c) observed for the pristine NCs solution. HAADF-STEM overview images (d, e) for Cd- and Zn-doped CsPbI₃ NCs after 6 hours, 5 and 10 days of exposure to air at 20 °C. White circles in (a) highlight the agglomeration of the NCs. The white arrow in (b) highlights grain boundaries formed because of agglomeration in the region marked by white rectangle in column (a) after 12 hours.

Characterization of planar defects via a combination of electron microscopy and MD simulations

To understand the nature of phase stabilization via doping by Cd and Zn, we analyzed the structural differences between the doped and undoped samples, prior to degradation, in more

detail. Pristine CsPbI₃ NCs were imaged along the [110] zone axes (Figure 2 (a)). Remarkably, in addition to the 'black' y-orthorhombic phase, identified for pristine samples, different crystallographic phases were found along the diagonal of the Cd and Zn-doped CsPbI₃ NCs. As can be seen from Figure 2 (b, c), these phases, highlighted by white lines, have a width of ~5 nm and are surrounded by [110]-oriented perovskites. For both types of doped NCs, the phases grew along the (-112) planes of perovskite orthorhombic structure. However, the atomic arrangement in these regions was found to be different for each material. For Cd-containing samples, an in-plane shift was only observed along one direction (Figure 2 (b), highlighted by arrows) parallel to the (1-10) γ-perovskite plane. It is clear from HAADF-STEM image (Figure 2 (b)), that in the defect region the Pb-containing columns of one perovskite layer are in between two Pb-containing columns of the other layers. On the other hand, for Zn-containing NCs, there is an in-plane ½ lattice shift of one perovskite unit along two perpendicular directions (Figure 2 (c), highlighted by arrows). This resulted in a structure where Pb-containing columns of one perovskite layer are in the center of the four Pb-containing columns of the other layer, as seen from Figure 2 (c). Additionally, after agglomeration of the NCs during the phase degradation these defects were still observed for the doped samples (Figure S4).

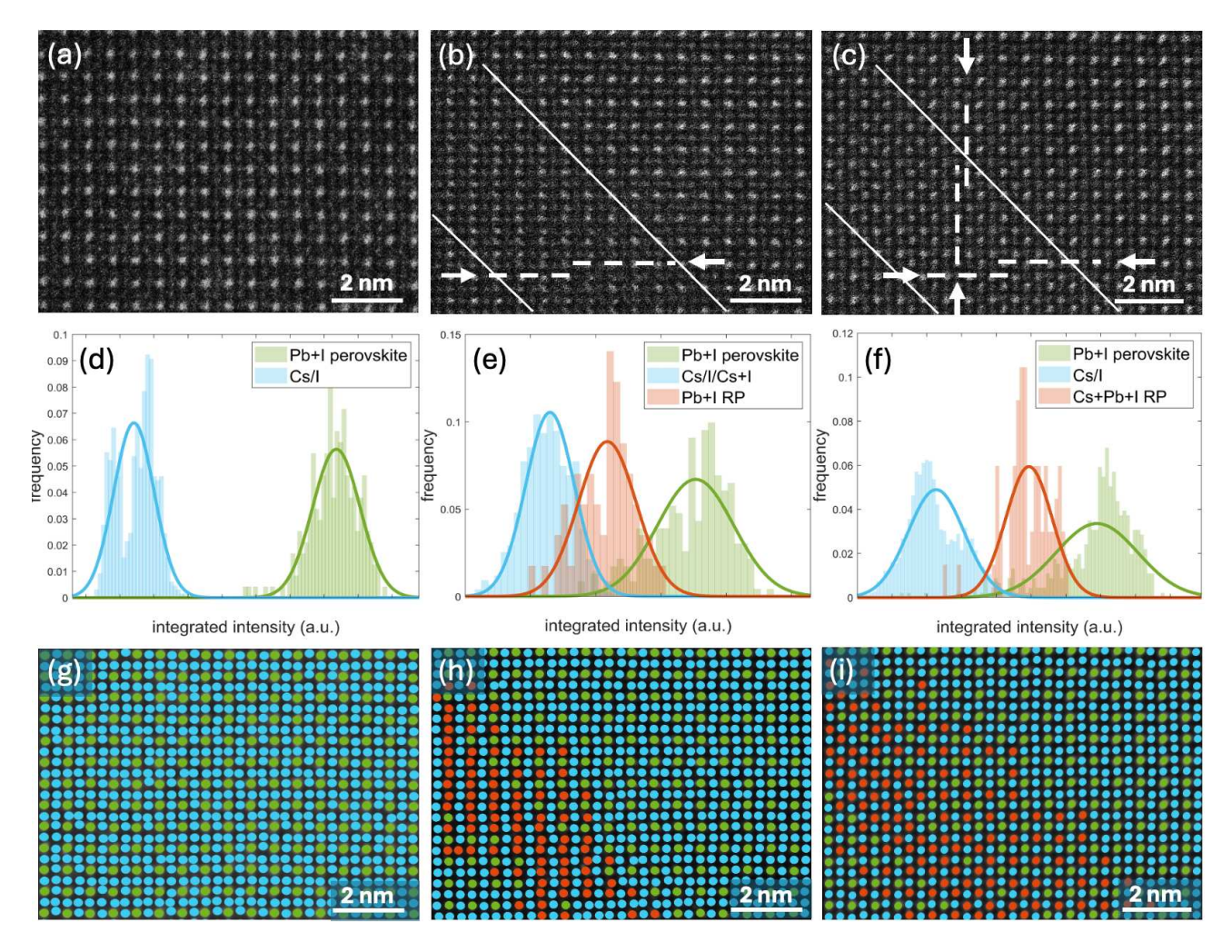


Figure 2. HAADF-STEM images of NCs for (a) undoped, (b) Cd-doped and (c) Zn-doped CsPbI₃ samples, acquired with a total electron dose of ~1500 e⁻/Å². White lines in (b), (c) highlight the areas with planar defects. White arrows in (b), (c) highlight half lattice shifts of [PbI₆]⁴⁻ octahedra in one and two directions for Cd and Zn-doped samples, respectively, resulting in planar defects formation. According to the analyzed integrated intensities in (d), (e), (f) quantitative maps (g), (h), (i) are plotted for HAADF-STEM images in (a), (b), (c). Peaks are assigned based on the columns in the middle of the perovskite or RP phase.

To further investigate the nature of the planar defects, we performed a quantitative analysis of the column intensities in the HAADF-STEM images (Figure 2 (d, e, f)), in which the intensities

scale with the atomic number of the elements in the sample (approximately proportional to Z^2)³⁵. A quantitative interpretation, based on statistical parameter estimation theory³⁶ indicates that for both Cd and Zn-containing NCs (Figure 2 (e, f, h, i)) there is a significant decrease of the column intensities in the defect region. If we assume a uniform sample thickness across the NCs, the difference in intensities of the atomic columns can be interpreted in terms of column composition. In the perovskite regions of the NCs, we assigned the columns with highest intensities (indicated in green) to Pb+I columns, while the atomic columns with total intensities corresponding to the lowest values (indicated in blue) were assigned to either Cs or I columns. In the defect region, we observed that the columns, which initially corresponded to the Pb+I columns (Figure 2 (g, h, i), green) in the perovskite lattice, showed a significant decrease in intensity as indicated in red (Figure 2 (h, i)). For the red-colored columns in the Cd- and Zn-doped samples (Figure 2 (h, i)), we therefore hypothesize that the columns in the defect regions include either 1) a large number of elements lighter than Pb or 2) Pb, Cs and I elements in a different ratio from that of the columns of the perovskite phase. By combining the observation of the stacking faults in the HAADF-STEM images (Figure 2 (b, c)) with the substantial decrease in the column intensities (Figure 2 (e, f)), we hypothesize that the as-found regions in the NCs would correspond to Ruddlesden-Popper (RP) phase defects. The interfaces between the assumed RP phases and perovskite phases were quantified in Figure S5. Our results indicate that the boundaries between the perovskites and defects are not atomically straight. This means that in a projection perpendicular to the one, observed with TEM, the length of the CsI layer varies across the NC (Figure S6).

To understand the role of the dopants in the formation of RP-like phase defects and the reason for the difference in phase stability between the three samples, we further investigated their structure. The presence of the RP phases has been proposed in the literature for doped CsPbBr₃^{37,38,39,40,41} but surprisingly, the underlying reasons and its formation pathway have not been fully understood. In the most general form, $A_{n+1}B_nX_{3n+1}$ RP phases are based on two distinct features, namely a corner-sharing CsPbI₃ perovskite layer and a planar CsI layer. In principle, the structure results from the intergrowth of the perovskite-type and rocksalt-type structures. Two ½ lattice shifts of the perovskite layers (Figure S1 (c)) in the RP structure maximize the distances between the I⁻ anions and between the Cs⁺ cations, resulting in a stable structure. The structure of this RP phase is in good agreement with our observations of defects found for the Zn-doped NCs. However, for the Cd-doped NCs, we observed the ½ lattice shift to be present only in one direction (Figure 2 (b)). To the best of our knowledge, such a structure has not been reported for MHPs yet. Homologous to RP, Dion-Jacobson⁴² structures are characterized by perovskite layers that are directly aligned without any shifts, thus, they are not suitable for the describing of the as-found planar defects in the Cd-doped sample. On the other hand, the observed one-shifted structure resembles A_nB_nO_{3n-2} found for oxide perovskites^{43,44}. Even though we do not establish the exact symmetry of the inter-perovskite layers, considering the origin of the new phase formation and following a general definition of RP phase, where perovskite layers alternate with CsI layers as well as due to the agreement in composition to Cs₂PbI₄, which will be shown later, we will herein also refer to this structure as RP-like phase.

The thermodynamic stability of the RP phases is typically determined by the exact number of perovskite layers (n)⁴⁵. As demonstrated in Table S2, the composition of the defect regions is close to Cs₂PbI₄, thus suggesting the presence of RP-like structures with n=1. There is an ongoing debate^{23, 46, 47} about which positions Cd/Zn atoms and other transition metal dopants occupy in the perovskite lattice or its derivatives. Our results show an increase of Zn and Cd signals in the RP

phases as indicated by the line profiles in Figure S7 (b, d) over 10 nm width. Although the amount of Zn²⁺ and Cd²⁺ is significantly less in the perovskite phase in comparison to the RP phase, we cannot fully exclude the presence of these dopants in the perovskite phase (Table S2). Based on these experimental results, we cannot establish the exact location of the dopants in both lattices. Notably, our results indicate that the significant differences in ionic radii between Zn²⁺ and Cd²⁺ play a critical role during the formation and determine the configuration of the RP-like phase.

Based on the EDX data, we expect the RP-like phases with n=1 for both samples. However, there are different possibilities when constructing models for the RP-like structures. CsI and perovskite layers can be oriented along different planes in the RP-like phases (Figure 3), relative to the original perovskite structure. We have investigated two orientations, which we will refer to as the 001- and 110-RP-like phases. For simplicity reasons, {001} and {110} notations include all equivalent crystallographic planes in the α -perovskite phase. To go beyond the interpretation of the 2D projected TEM data and to confirm a 3D model of the RP phases and the interface with the perovskite lattice, we performed MD simulations at room temperature and atmospheric pressure. To conduct long MD simulations (400 ps) for large simulation cells (up to 10000 atoms) with firstprinciples accuracy, we trained a machine learning potential (MLP) based on the MACE architecture⁴⁸ using CP2K⁴⁹ ab initio data through Psiflow⁵⁰ (Computational details in Methods section). Although the experimental projections (z-direction) of 001- and 110- RP-like phases are expected to be identical, there is a significant difference in the projections along x- and y-directions for 001 and 110-RP-like structural models (Figure 3). We, therefore, performed image simulations with the MULTEM software⁵¹ using the average structure obtained from MD simulations as an input (Figure 4 (a, c, f, h)). Surprisingly, the difference between the simulated images of 001- and 110-one-shift RP-like structures along the z-direction is distinct. The observed visual elongation

of the atomic columns in Figure 4 (b) resulting in broad intensity distribution for both Pb+I and Cs+I (Figure S8 (a, b)) does not match with well-defined atomic columns found in the experimental images (Figure 4 (e), Figure S8 (c)) of one-shift planar defect. On the other hand, the 110-one-shift RP-like structural model agrees well with the experiment, as seen from the simulated results (Figure 4 (d)). Moreover, from the experimental images of the one-shift RP-like phase (Figure 4 (e)), a zigzag arrangement of Pb+I and Cs+I columns is evident. To prove it quantitatively, we have plotted atomic columns positions (Figure S9 (a)). This arrangement is reproduced by the image simulations based on our MD data (Figure 4 (e), Figure S9 (b, c)) for two types of 110-one-shift RP-like phases, i.e. pure and with Cd-incorporated into the positions of Pb (coordination number=6). The MD averaged structures contain a small offset between the Pb+I columns as well as between Cs+I columns of different perovskite layers, i.e. the perovskite layers do not perfectly project on the same line. Therefore, a zigzag line is formed when projecting Pb+I or Cs+I columns belonging to one perovskite layer and Pb+I or Cs+I columns belonging to another. This reduces the repulsion between I- anions of neighboring perovskite layers, which is the destabilizing factor of the one-shift RP phases.

Unlike the one-shift RP structures, a comparison between the simulated images for both 110-and 001-structures with the experimental HAADF-STEM images (**Figure 4** (**g**, **i**, **j**)) for the two-shift RP-like phase shows excellent visual agreement. To further quantify this comparison, we measured intercolumn distances by statistical parameter estimation implemented in StatSTEM³⁶, which revealed a good match (Figure S10). Hence, it is not possible to rule out 110- or 001-two-shift RP structure based only on the TEM data.

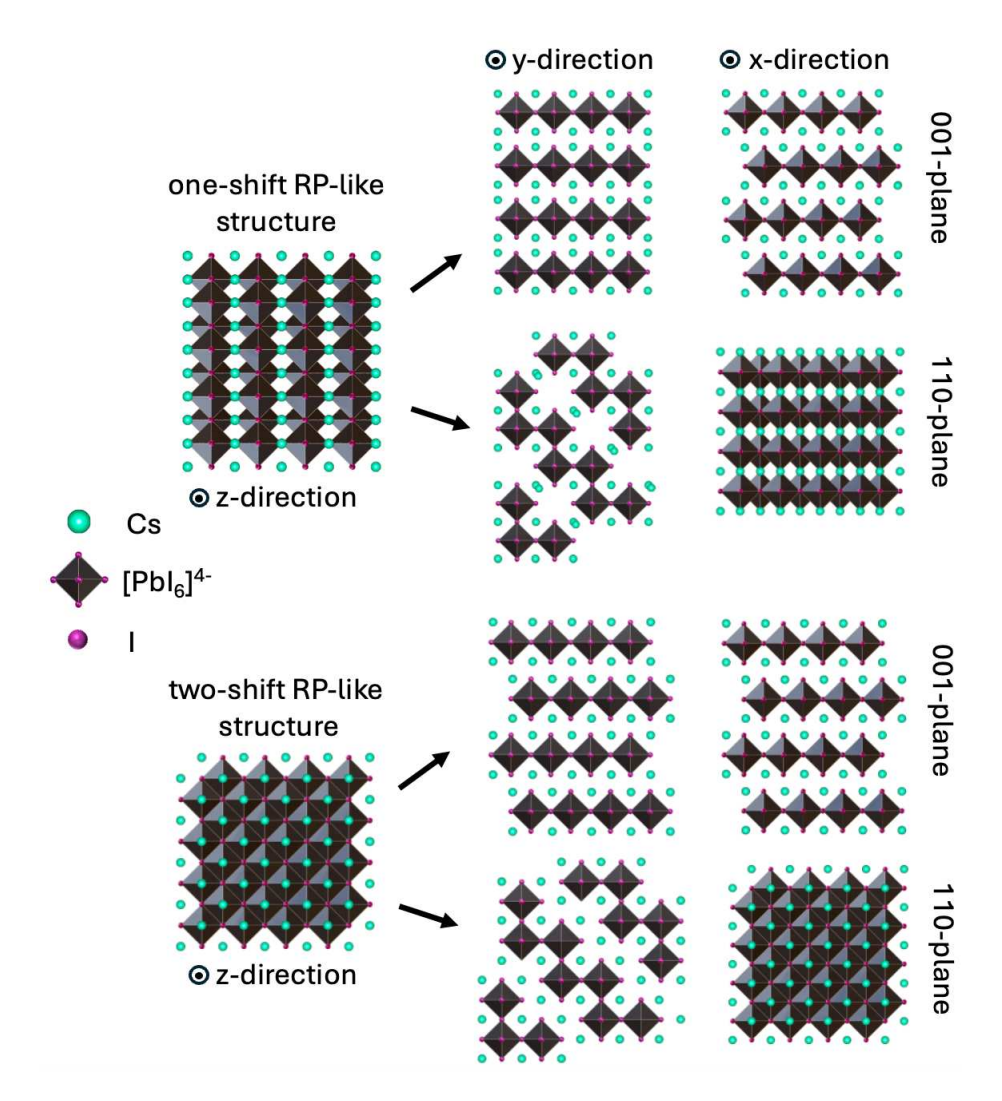


Figure 3. Schematic depiction of the experimental projections along z-direction as well as differences in projections along the x- and y-directions of one-shift and two-shift RP structures with CsI layers along the 001- or 110-planes.

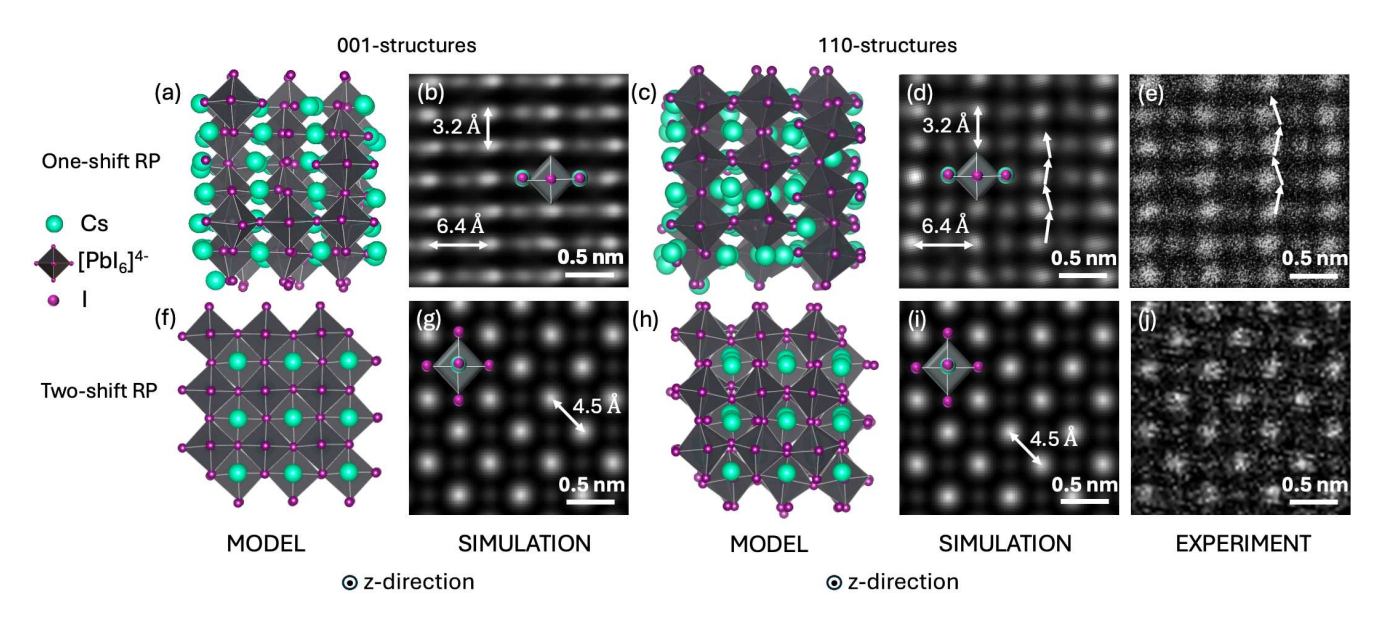


Figure 4. MD averaged structures (a, c, f, h), MULTEM simulated images (b, d, g, i), experimental (e, j) HAADF-STEM images of 001 and 110-RP-like phases found for Cd-modified and Zn-modified CsPbI₃ samples. Zigzag arrangements of [PbI₆]⁴⁻ octahedra for one-shift RP phase are highlighted by white arrows (d, e).

Using MD simulations we estimated the energy of all structures at room temperature, which is a direct indication of their relative stability. For the two-shift RP phase, the 110-structure is 3.8 kJ/mol per formula unit more stable than the 001-structure. For the one-shift RP-like structure, the 001-structure remained not stable during MD simulations and ended up in the two-shift RP phase, whereas the 110 one-shift structure did remain stable. From this, we conclude that for both types of RP-phases, 110-structures are the expected structures in the experiments. Once the MD simulated structural models **Figure 4 (c, h)** were validated, we can fully interpret the intensities of the atomic columns in **Figure 2 (b, c, e, f)**. A full description is provided in Figure S11.

After finding the best match between MD models and experiments when considering RP phases without doping, we investigated the positions of the dopants in these phases. As mentioned,

understanding of the feasibility of Pb/Cs substitution by Zn/Cd in RP phases cannot be obtained through experimental measurements; MD simulations were, therefore, performed. We considered Cs⁺ substitution by Zn²⁺ or Cd²⁺ in the 110-RP-like phases which are found to be the preferred RP structures without doping (Figure S12). Because of the charge difference between Cs⁺ and Zn²⁺/Cd²⁺, two Cs⁺ cations are expected to be replaced by one Zn²⁺ or Cd²⁺ cations. Additionally, we considered substitution of one Pb²⁺ by one Zn²⁺/Cd²⁺. Since the RP phase has I⁻ anions that are only bound to one Pb²⁺ cation, we also analyzed the substitution of a Pb²⁺ with a Zn²⁺ or Cd²⁺ that does not have the octahedral iodine coordination, but has a lower coordination, i.e. with 5 or 4 I⁻ neighbors.

Figure S12 (a) shows the average structures obtained via MD simulations for 380 ps at 300 K and 0.1 MPa for Cd-doped 110-one-shift RP-like phase. When starting from Cd²⁺ cations that are coordinated by 5 or 4 I⁻ in one-shift RP-like phase, in both cases the MD simulations resulted in CdI₄ tetrahedra, indicating that Cd incorporation can lead to breaking of some Pb-I/Cd-I bonds (Figure S12 (a), option 3 and 4) as indicated by orange circles. Cs substitutions by Cd can result in bond breaking and consequently, in tetrahedral coordination, too. At the same time, a 6-coordinated Cd-cation in a Pb positions remains stable in MD simulations with no bond breaking. Nevertheless, the stability of the as-discussed options highly depends on the local concentration of the dopant. This can be concluded from the simulations performed for Cd-incorporated 110-one-shift RP-like structures (Table S3). Here, the stable options are a substitution of Pb by 1 Cd per 64 formula units with keeping 6 or 5 I⁻ neighbours, while in the case with 6 Cd per 64 formula units, MD simulations reveal that Cs substitution by Cd becomes more stable.

Figure S12 (b) shows four options of the average structures obtained via MD simulations for 180 ps at 300 K and 0.1 MPa for Zn-doped 110-two-shift RP phase. When starting from different initial coordination of Zn cations in Cs or Pb positions, Zn incorporation always results in tetrahedral coordination, accompanied by Pb-I, Zn-I bond breakage. Due to the smaller size of Zn²⁺ compared to Pb²⁺, Zn²⁺ pulls certain I⁻ atoms away from neighboring Pb²⁺. For the case of Pb substitution by Zn in the RP phase the tetrahedral coordination is more energetically favorable than for Pb (see SI, coordination environment of Zn). Based on these results, it is difficult to estimate which position is more preferential for Zn because all the discussed options are 100% stable, however, the affinity to be coordinated by four halides is supported by our data (Figure S12).

From these results, we conclude that position of Cd in one-shift RP-like lattice depends significantly on a local concentration of Cd in the unit cell. Moreover, Zn²⁺ cations presumably have no preferred position in the two-shift RP lattice, but certainly have a preference for tetrahedral coordination in the RP-like phase.

Mechanistic understanding of the improved phase stability of doped NCs and the role of Ruddlesden-Popper-like planar defects

After characterizing the precise structures of the RP-like phases, we discuss the underlying reasons for the improved phase stability. Two aspects are hereby important: the increased kinetic stability due to the presence of the RP-like structures and the chemical influence of the dopants. The Pb-I-Pb bond angle distribution is an indication of the kinetic stability of the perovskite phase since the Pb-I-Pb bond angle changes from approximately 180° to 90° when going from the α -phase of CsPbI₃ to the δ phase⁵². Based on the precise structures of the RP-like phases that were

determined from the synergy between experiment and MD modeling we were able to simulate Pb-I-Pb bond angles for the RP structures found in doped samples, including such MD simulations for the RP/perovskite interface. Hence, we constructed atomistic models of the interfaces between the perovskite and RP phases and simulated TEM images which are in a good agreement with the experimental results (Figure 5 (a, b, c, d)). The interface between the one-shift RP-like structure and the perovskite (Figure S13 (a, b)) has not been reported in literature for MHPs. Even though the [PbI₆]⁴⁻ octahedra in the one-shift RP phase are located close to each other, leading to the slight offsets in atomic positions (Figure S9), the interface between the perovskite and 110-one-shift RP phase is stable in MD simulations. Moreover, the incorporation of Cd²⁺ cations can aid to reduce the strain created due to the close location of atoms at the interface between one-shift RP-like and perovskite phases, because it is probable for Cd²⁺ to change the coordination environment to 4 or 5 I⁻ anions when substituting Pb²⁺ or Cs⁺ (Figure S13 (b)). A schematic depiction of the interface between two-shift RP and perovskite phases is shown in Figure S13 (d, e). As described earlier, the columns of Cs+I+Pb in the two-shift RP phase are in a center of four Pb+I atomic columns which originally corresponded to the perovskite phase. The intensities of these Cs+I+Pb columns in the two-shift RP phase at interface with perovskites have some variations, which can be explained by the CsI layer length variation (Figure 5 (c, d), Figure S6). If the CsI layer variation is not considered, a drastic change of the intensities at RP/perovskite interface is observed (Figure S14, red arrow).

According to MD simulations (**Figure 5 (e)**), the γ -phase has on-average Pb-I-Pb bond angles of 152.7°, whereas for the one-shift RP-like phase, observed for Cd-doped MHP NCs, the value equals to 154.2° (154.3° at the interface) and for the two-shift RP phase, observed for Zn-doped NCs, the angle is 155.7° (155.6° at the interface). The found tendency correlates well with the phase

stability measurements (**Figure 1**), since the Zn-doped material demonstrated the highest phase stability, and the Cd-doped material surpassed the unmodified CsPbI₃. Additionally, the chemical influence of the substituents on the phase stability cannot be overlooked. The presence of dopants can alter bonding strength (Zn-I/ Cd-I vs. Cs-I and Pb-I) as well as induce lattice distortions, which can in turn modify the iodine diffusion pathway. Such changes could reduce the mobility of iodine ions, which plays a key role in the phase transition from the α-phase to the δ-phase of CsPbI₃⁵³. However, a more detailed understanding of the chemical influence requires precise knowledge of the dopants' positions within both the perovskite and RP-like lattices, which could be explored in a future dedicated study. Moreover, the thermodynamic stability of modified samples is different. The Cd-containing sample has a one-shift RP-like phase, which has a higher energy than the two-shift RP phase of the Zn-containing sample. Hence, the thermodynamic stability of the Zn-modified sample is expected to be higher than that of the Cd-modified sample, as observed experimentally.

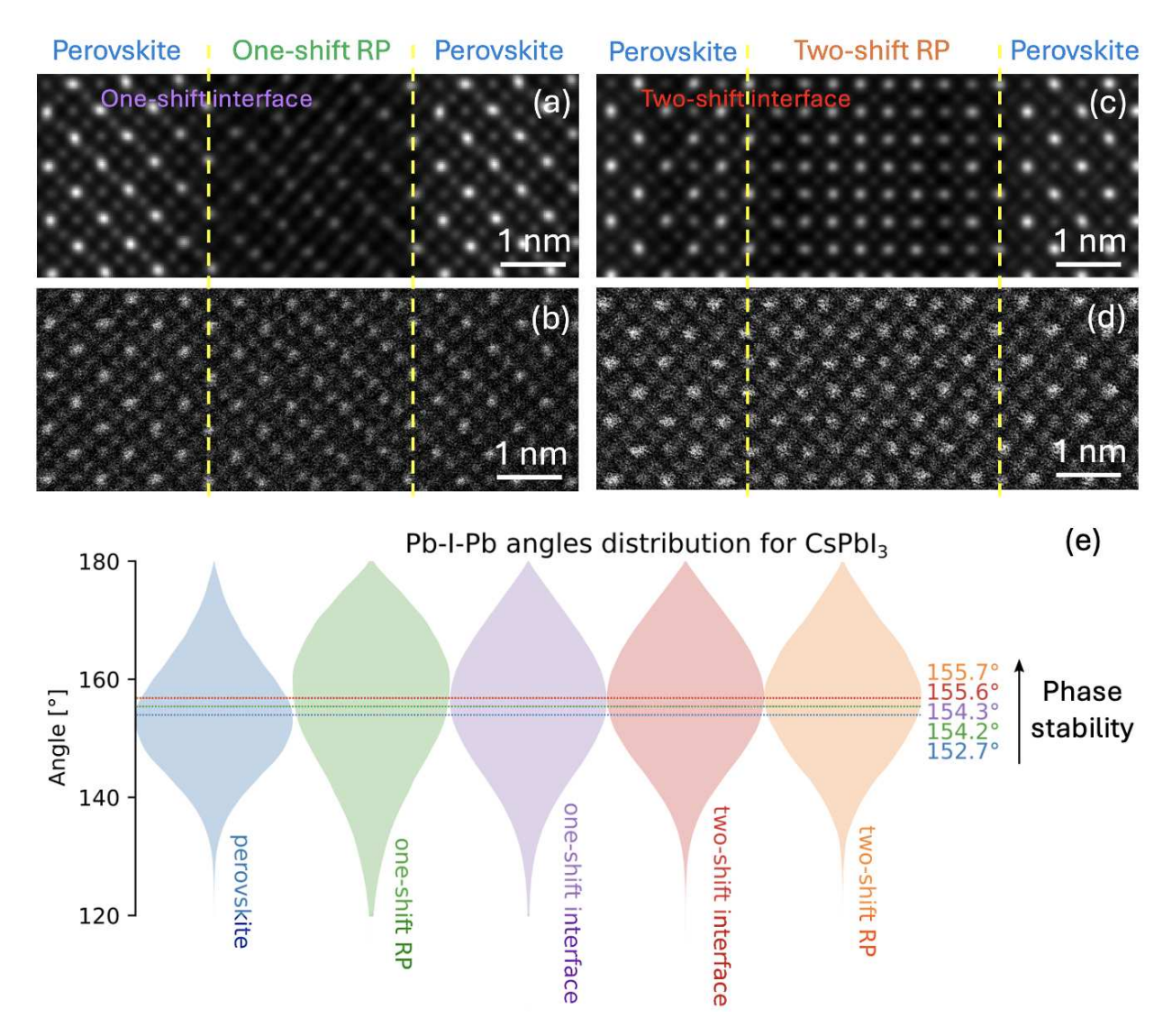


Figure 5. Simulated MULTEM (a, c) and experimental HAADF-STEM (b, d) images of the interfaces for the NCs with RP defects found in (a, b) Cd-modified and (c, d) Zn-modified CsPbI₃ samples. Simulated images (a, c) with 110-RP structure which include variation of the CsI layer length in the out-of-plane direction of the structure. Pb-I-Pb bond angle distribution (e) of five different structures resulting in a phase stability difference. The average bond angle is indicated by the dotted lines and is an indication of the kinetic stability of the structure, *i.e.* the higher the angle the more stable the structure.

The insights obtained about the formation of RP-like defects in this work could guide the synthesis of ultra-stable black-CsPbI₃ NCs. There are two general requirements for the formation of the RP-like phases, starting from the perovskite phase. The first requirement is an external stimulus for the perovskites octahedra to grow in a shifted manner. This can, for example, be a lattice strain due to the presence of dopants. The second requirement is that after the introduction of lattice shifts, the growth proceeds with the CsI plane, thus requiring an excess of Cs⁺ and I⁻ ions. If both conditions are satisfied, the perovskite layers shift with respect to each other in one or two directions, i.e. one-shifted and two-shifted RP-like structures are formed.

Zn and Cd have a different effect on the RP-like phases formation from the perovskite phase. For the Zn-doped sample, a two-shift RP phase was formed, whereas for the Cd-doped sample, a one-shift RP-like phase was observed. Among these, a two-shift RP phase is energetically preferred. However, when forming the RP phase for the Cd-containing sample, the second shift is kinetically trapped in the one-shift structure. A schematic representation of the perovskite lattice evolution towards the one-shift and two-shift RP phases in presence of the dopant with the corresponding in- and out-of-plane shifts is shown in Figure S15. Due to the smaller ionic radii of Cd²⁺ in comparison to Pb²⁺, Cd does not perfectly fit into the 3D Pb-I framework. Thus, at higher concentrations of Cd, the RP phase formation is likely to be promoted due to the build-up of strain. Cd²⁺ can also remain undercoordinated in both Cs and Pb positions. Therefore, fewer I⁻ anions are required for the RP structure formation than in case of 6 I⁻ coordinated Pb for pure RP-like phase. In addition, the presence of undercoordinated Cd leads to fewer atoms at the interface, thereby removing strain between the perovskite and RP phases. Zn²⁺ incorporation into Cs positions is accompanied either with an I-, which takes up more space than the substituted Cs+ or by the removal of a second Cs⁺ cation for charge compensation reasons. Consequently, strain is

transferred onto the octahedral framework, which could initiate the growth of shifted Pb²⁺ cations that are further apart compared to the ideal perovskite structure. For the case with Zn²⁺ substituting Pb²⁺ such strain may arise from the large difference in ionic radii between these two cations. The higher the Zn concentration, the more likely the first step of RP phase formation occurs. In case of Zn²⁺ substituting Cs⁺, less Cs⁺ cations are required to form the RP phase, since two Cs⁺ have to be substituted for charge compensation. On the other hand, in the case of Pb²⁺ substitution, Zn²⁺ remains undercoordinated, meaning that less extra I anions are necessary to form the RP-like phase, which can, similarly to the Cd-case, promote the RP phase formation. This way both options of Cd as well as Zn incorporation are facilitating the RP phase formation.

CONCLUSIONS:

In summary, we have conducted a synergistic experimental and computational study to understand how addition of Zn²⁺ and Cd²⁺ during the hot-injection synthesis of CsPbI₃ NCs influences its phase stability. TEM measurements revealed that the degradation of γ-CsPbI₃ led to NCs agglomeration and a subsequent structural transformation into yellow phase microtubes/nanowires. In addition, for two modified samples enhanced phase stability of black-CsPbI₃ was shown. Both transition metals were identified as key factors in the formation of the planar defects with specific atomic arrangements, found for two modified materials. One-shift RP stacking faults, found in Cd-doped sample, were shown and characterized for the first time for MHPs. MD simulations demonstrated that a tetrahedral coordination of Zn in the two-shift RP phase is most beneficial, independently if Cs⁺ or Pb²⁺ cations are substituted. On the contrary, the coordination of Cd in the one-shift RP-like phase may vary significantly with its concentration. Our results suggest that RP phase formation due to Zn- and Cd-incorporation is promoted by lattice

strain introducing shifts of neighboring [PbI₆]⁴⁻ octahedra and mitigates the need for additional Cs⁺ and I⁻ ions to continue the lattice growth. An improvement in phase stability, observed for Zn and Cd-modified CsPbI₃, is associated with the as-described RP-like stacking faults due to decreased kinetics, as determined by increased average Pb-I-Pb bond angles. Overall, our study provides significant insights through a comprehensive modeling and experimental study for stabilizing perovskite NCs.

METHODS:

Materials synthesis

1.1 Preparation of Cs-oleate precursor

To create Cs-oleate precursors, a mixture was prepared in a 25 mL three-neck round-bottom flask by combining 400 mg of Cs₂CO₃, 15 mL of 1-octadecene (ODE), and 1.725 mL of oleic acid. The flask was subjected to vacuum degassing at 120°C for 60 minutes under constant stirring until all the Cs₂CO₃ had completely dissolved, resulting in a clear solution. The mixture was then heated to 150°C under a nitrogen atmosphere and annealed for an additional 30 minutes. The resulting Cs-oleate solution was stored under a nitrogen environment for future use.

1.2 Synthesis of CsPbI₃ NCs

The preparation protocol was adapted from⁵⁴. 0.703 mmol PbI₂ (324.1 mg), 0.022 mmol of PbBr₂ (8.1 mg), 10 mL of ODE, 2 mL of oleic acid and 2 mL of oleylamine were loaded into a 25 mL three-neck flask and dried under vacuum conditions for 1 hour at 120°C for full precursors dissolution. The reaction atmosphere was then switched to nitrogen, and the temperature was set at 170°C. Once the temperature was stabilized, 1.6 mL of preheated Cs-oleate solution was swiftly

injected into the precursor mixture. The reaction was rapidly quenched within 10 seconds using an ice water bath to halt further NCs growth.

1.3 Purification of the NCs

The purification procedure was adapted based on⁵⁵. The crude reaction product was collected in a 50 mL centrifuge tube followed by centrifugation at 8500 rpm for 10 min. The top supernatant part, which contained surface ligands, solvents and unreacted precursors, was discarded carefully. The remaining precipitate was then dispersed in 5 mL hexane by vigorously shaking the vial. Following this, methyl acetate, nonsolvent, was added into the hexane dispersion of the NCs and mixed by shaking. The mixture was immediately centrifuged at 8500 rpm for 30 seconds and the top supernatant was discarded. The bottom part was re-dispersed in 2.5 mL of hexane, centrifuged at 4000 rpm for 3 minutes and the final top supernatant was collected and stored under refrigeration at 4 °C for future use.

1.4 Zn-doped CsPbI₃ NCs synthesis and purification

The procedure for doping was adapted from²³. 0.703 mmol of PbI₂ (324.1 mg), 0.022 mmol of PbBr₂ (8.1 mg), 0.725 mmol of ZnI₂ (231.4 mg), 10 mL of ODE, 2mL of oleic acid and 2 mL of oleylamine were loaded into a 25 mL three-neck flask. The subsequent synthesis and purification steps followed the same procedure as described above for CsPbI₃ NCs.

1.5 Cd-doped CsPbI₃ NCs synthesis and purification

0.703 mmol of PbI₂ (324.1 mg), 0.022 mmol of PbBr₂ (8.1 mg), 0.725 mmol of CdI₂ (265.5 mg), 10 mL of ODE, 2mL of oleic acid and 2 mL of oleylamine were loaded into a 25 mL three-neck flask. The subsequent synthesis and purification steps followed the same procedure as described above for CsPbI₃ NCs.

TEM characterization

As-prepared solutions of undoped, Zn-doped and Cd-doped CsPbI₃ NCs were drop-casted onto a carbon-coated copper grid inside a glove box. The solvent (hexane) was allowed to evaporate prior to imaging.

2.1 High angle annular dark field scanning transmission electron microscopy imaging (HAADF-STEM imaging) and energy dispersive X-ray spectroscopy (EDX)

HAADF-STEM images were acquired with the total dose of ~1500 e⁻/Å² using a probe-corrected Thermo Fisher Titan Themis Z microscope operated at 300 kV with a probe semi-convergence angle of 21 mrad and equipped with a Super-X EDX system. For composition analysis, EDX spectra in STEM mode were acquired within ~600 seconds at 30 pA for low magnification maps and ~90 seconds at 100 pA for high magnification maps.

2.2 Quantitative analysis with StatSTEM

Quantitative analyses of column intensities and column-to-column distances were performed using the StatSTEM software³⁶. For this purpose, a parametric model was used which consists of a sum of Gaussians, each centered on the atomic column positions. The unknown parameters, i.e. the positions, width and height of each Gaussian, were estimated by fitting this model to the experimental images using a non-linear least squares optimization. Based on the estimated parameters, the total scattered intensities and the locations of all atomic columns were determined. Based on the total scattered intensity of the known atomic columns for the perovskite and RP phase, the mean and standard deviation of the corresponding normal distributions have been estimated. This prior knowledge could then be used to determine the probability that a column in the interface region belongs to the perovskite or RP phase.

2.3 HAADF-STEM images simulations with MULTEM

HAADF-STEM image simulations were performed using the MULTEM package⁵¹. An acceleration voltage of 300 kV, a semi-convergence angle of 21 mrad and a pixel size of 0.3 Å were chosen and averaging over 30 unique phonon configurations was performed. The full set of simulation settings is listed in Supplementary Table S6.

Computational details

3.1 Structure generation

All structures were generated using a few input structures and Python scripts, which are available at https://doi.org/10.5281/zenodo.14600071. These generated structures were used as initial structures for the MD simulations and can also be found via this link. The average structure during a MD simulation was used to simulate its TEM image and compare it with the experiment. More information can be found in SI, Structure generation.

3.2 Molecular dynamics simulations

Yaff was used to perform the NPT MD simulations⁵⁶. The force evaluations were performed with a machine learning potential (MLP) trained on density functional theory (DFT) energies and forces. The timestep was set to 2 fs, and all simulations were 200 or 400 ps long. The first 20 ps of each MD simulation was used as equilibration time. The temperature was set to 300 K and controlled with a Langevin thermostat⁵⁷ using a time constant of 100 fs. The pressure was set to 0.1 MPa and controlled with a Langevin barostat⁵⁸ using a time constant of 1 ps. The complete workflow containing all MD simulations and post-analysis Python scripts is available at https://doi.org/10.5281/zenodo.14600071. Only the assessment of the stability of the one-shift RP structures for a specific MD simulation was performed manually. More information can be found in SI, MD simulations.

3.3 MLP development via active learning

Psiflow version 3.0.2⁵⁰ was used to train the MLP via an active learning loop. Each iteration occurs in three steps. First, the *ab initio* energy and forces are calculated for a set of structures. Second, a new MLP is trained on the generated *ab initio* data set. Third, short MD simulations are performed with the new MLP to generate new input structures. These structures are then used in the following iteration, to increase the training dataset with more ab *initio* energies and forces. CP2K was used to perform the *ab initio* calculations⁴⁹. PBE-D3(BJ)^{59,60} was set as XC functional, and a combination of Gaussian and Plane Wave (GPW) was used as the basis set. The MACE architecture⁴⁸ with a cut-off radius of 7 Å was used to train the MLP. Psiflow utilizes openMM⁶¹ to perform the NPT MD simulations during active learning. The complete overview of the CP2K, MACE, openMM, and psiflow settings can be found in the psiflow input files available at https://doi.org/10.5281/zenodo.14600071. More information can be found in SI, MLP development via active learning.

ASSOCIATED CONTENT

Supporting Information

The Supporting Information is available free of charge at DOI:

Structural models of black and yellow CsPbI₃, RP Cs₂PbI₄, phase analysis, EDX for average composition quantification, probabilities analysis for the atoms belonging to either RP or perovskite phase close to the interfaces, scheme about CsI layer variation in RP structure, EDX at high magnification, line profiles for simulated and experimental images, atomic coordinates plots, intercolumn distances calculated for the experimental images, explanation of the column compositions in RP-like phases, RP-perovskite interface optimization, MD snapshots of the RP

structures with dopants and their stability, RP-perovskite interface optimization, explanation about

coordination environment investigation, details of the HAADF-STEM images simulations,

generation of the structures for MD simulations, details of the MD simulations, details of the MLP

training via active learning, comparison of the universal and specific machine learning potentials.

All the structures generated in this work are provided at https://doi.org/10.5281/zenodo.14600071.

AUTHOR INFORMATION

Corresponding Author

* Sara Bals: sara.bals@uantwerpen.be

Author Contributions

I.S. performed and analyzed the STEM experiments. T.B. trained the MLP, conducted the MD

simulations and analyzed the results. A.D.B. contributed to the intensity analysis and the

MULTEM simulations. N.S. contributed to the analysis of the STEM results. B.P. synthesized the

NCs. J.H., V.V.S., S.V.A. and S.B. coordinated the research work. I.S. and S.B. wrote the

manuscript. All authors contributed to reviewing and editing the manuscript and have given

approval to the final version of the manuscript.

Funding Sources

ACKNOWLEDGMENT

The authors acknowledge financial support from the Research Foundation – Flanders (FWO)

through a doctoral fellowship to I.S. (FWO-SB Grant No. 1SHA024N) and a postdoctoral

fellowship to N.J.S. (FWO Grant No. 12AAO25N). The authors acknowledge financial support

from iBOF-21-085 PERSIST and the Research Foundation-Flanders (FWO) through project

27

fundings (G0A7723N). V.V.S. acknowledge funding from the Research Board of Ghent University (BOF). The computational resources and services used in this work were provided by the VSC (Flemish Supercomputer Center), funded by the Research Foundation-Flanders (FWO) and the Flemish Government–department EWI.

ABBREVIATIONS

High-angle annular dark-field HAADF, scanning transmission electron microscopy STEM, light-emitting diode LED, metal halide perovskites MHP, Ruddlesden-Popper (RP), nanocrystals NCs, energy-dispersive X-ray spectroscopy EDX, machine learning ML, machine learning potential MLP, molecular dynamics MD

REFERENCES

- (1) Stranks, S.D.; Snaith, H.J. Metal-halide perovskites for photovoltaic and light-emitting devices. *Nature Nanotech.* **2015**, 10, 391-402.
- (2) Chen, Q.; De Marco, N.; Yang, Y. (Michael); Song, T.-B.; Chen, C.-C.; Zhao, H.; Hong, Z.; Zhou, H.; Yang, Y. Under the Spotlight: The Organic–Inorganic Hybrid Halide Perovskite for Optoelectronic Applications. *Nano Today* **2015**, 10 (3), 355–396.
- (3) Sutton, R.J.; Filip, M.R.; Haghighirad, A.A.; Sakai, N.; Wenger, B.; Giustino, F.; Snaith, H.J. Cubic or Orthorhombic? Revealing the Crystal Structure of Metastable Black-Phase CsPbI₃ by Theory and Experiment. *ACS Energy Lett.* **2018**, 3, 8, 1787-1794.
- (4) Wang, Y.; Dar, M. I.; Ono, L. K.; Zhang, T.; Kan, M.; Li, Y.; Zhang, L.; Wang, X.; Yang, Y.; Gao, X.; Qi, Y.; Grätzel, M.; Zhao, Y. Thermodynamically Stabilized β-CsPbI₃-Based Perovskite Solar Cells with Efficiencies >18%. *Science* **2019**, 365 (6453), 591–595.

- (5) Wang, J.; Che, Y.; Duan, Y.; Liu, Z.; Yang, S.; Xu, D.; Fang, Z.; Lei, X.; Li, Y.; Liu, S. 21.15%-Efficiency and Stable γ-CsPbI₃ Perovskite Solar Cells Enabled by an Acyloin Ligand. *Adv. Mater.* **2023**, 35, 12, e2210223.
- (6) Zhang, H.; Debroye, E.; Vina-Bausa, B.; Valli, D.; Fu, S.; Zheng, W.; Virgillio, L.; Gao, L.; Frost, J.; Walsh, A.; Hofkens, J.; Wang, H.; Bonn, M. Stable Mott Polaron State limits the charge density in lead halide perovskites. *ACS Energy Lett.* **2023**, 8(1), 420-428.
- (7) Zhang, H.; Debroye, E.; Steele, J.; Roeffaers, M.; Hofkens, J.; Wang, H.; Bonn, M. Highly mobile large polarons in black phase CsPbI₃. *ACS Energy Lett.* **2021**, 6(2), 568-573.
- (8) Chen, L.-C.; Chang, Y.-T.; Tien, C.-H.; Yeh, Y.-C.; Tseng, Z.-L.; Lee, K.-L.; Kuo, H.-C. Red Light-Emitting Diodes with All-Inorganic CsPbI₃/TOPO Composite Nanowires Color Conversion Films. *Nanoscale Res. Lett.* **2020**, 15 (1), 216.
- (9) Yi, C.; Liu, C.; Wen, K.; Liu, X.-K.; Zhang, H.; Yu, Y.; Fan, N.; Ji, F.; Kuang, C.; Ma, B.; Tu, C.; Zhang, Y.; Xue, C.; Li, R.; Gao, F.; Huang, W.; Wang, J. Intermediate-Phase-Assisted Low-Temperature Formation of γ-CsPbI₃ Films for High-Efficiency Deep-Red Light-Emitting Devices. *Nat. Commun.* **2020**, 11 (1), 4736.
- (10) Marronnier, A.; Roma, G.; Boyer-Richard, S.; Pedesseau, L.; Jancu, J.-M.; Bonnassieux, Y.; Katan, C.; Stoumpos, C. C.; Kanatzidis, M. G.; Even, J. Anharmonicity and Disorder in the Black Phases of Cesium Lead Iodide Used for Stable Inorganic Perovskite Solar Cells. *ACS Nano* **2018**, 12 (4), 3477–3486.
- (11) Straus, D. B.; Guo, S.; Cava, R. Kinetically Stable Single Crystals of Perovskite-Phase CsPbI₃. J. Am. Chem. Soc. **2019**, 141, 29, 11435-11439.

- (12) Kweon, K.E.; Varley, J.; Ogitsu, T.; Wan, L. F.; Shelby, M.; Song, Z.; Ellingson, R.J.; Yan, Y.; Lee, J. R. Influence of external conditions on the black-to-yellow phase transition of CsPbI₃ based on first-principles calculations: Pressure and Moisture. *Chem. Mater.* **2023**, 35 (6), 2321-2329.
- (13) Dastidar, S.; Hawley, C.J.; Dillon, A.D.; Gutierrez-Perez, A.D.; Spanier, J.E.; Fafarman A.T. Quantitative phase-change thermodynamics and metastability of perovskite-phase cesium lead iodide. *J. Phys. Chem. Lett.* **2017**, 8 (6), 1278-1282.
- (14) Lin, C.; Zhang, Y.; Gao, M.; Lin, J.; Le, H.K.D.; Lin, Z.; Yang, P. Controlling the phase transition in CsPbI₃ nanowires. *Nano Lett.* **2022**, 22 (6), 2437-2443.
- (15) Liu, J.; Hao, X.; van Huis, M. A.; Fan, Z. Microscopic mechanism of water-assisted diffusional phase transitions in inorganic metal halide perovskites. *J. Phys. Chem.* **2024**, 161 (17), 174705.
- (16) Lin, Z.; Zhang, Y.; Gao, M.; Steele, J.A.; Louisia, S.; Yu, S.; Quan, L.N.; Lin, C.; Limmer, D.T.; Yang, P. Kinetics of moisture-induced phase transformation in inorganic halide perovskite. *Matter* **2021**, 4 (7), 2392-2402.
- (17) Arslanova, K.; Ganswindt, P.; Lorenzen, T.; Kostyurina, E.; Karaghiosoff, K.; Nickel, B.; Muller-Caspary, K.; Urban, A. S. Synthesis of Cs₃Cu₂I₅ Nanocrystals in a continuous flow system. *Small* **2024**, 20 (44), 2403572.
- (18) Steele, J. A.; Jin, H.; Dovgaliuk, I.; Berger, R. F.; Braeckevelt, T.; Yuan, H.; Martin, C.; Solano, E.; Lejaeghere, K.; Rogge, S. M. J.; Notebaert, C.; Vandezande, W.; Janssen, K.P.F.; Goderis, B.; Debroye, E.; Wang, Y.; Dong, Y.; Ma, D.; Saidaminov, M.; Tan, H.; Lu, Z.; Dyadkin,

- V.; Chernyshov, D.; Speybroeck, V. V.; Sargent, E.H.; Hofkens, J.; Roeffaers, M.B.J. Thermal unequilibrium of strained black CsPbI₃ thin films. *Science* **2019**, 365, 6454, 679-684.
- (19) Steele, J.; Prakasam, V.; Huang, H.; Solano, E.; Chernyshov, D.; Hofkens, J.; Roeffaers, M. Trojans That Flip the Black phase: impurity-driven stabilization and spontaneous strain suppression in γ-CsPbI₃ perovskite. *J. Am. Chem. Soc.* **2021**, 143(28), 10500-105008.
- (20) Ahmed, G. H.; Yin, J.; Bakr, O. M.; Mohammed, O. F. Successes and Challenges of Core/Shell Lead Halide Perovskite Nanocrystals. *ACS Energy Lett.* **2021**, 6 (4), 1340-1357.
- (21) Wu, Y.; Jia, R.; Xu, J.; Song, L.; Liu, Y.; Zhang, Y.; Ullah, S.; Dai, J. Strategies of Improving CsPbX₃ Perovskite Quantum Dots Optical Performance. *Front. Mater.* **2022**, 9.
- (22) Akkerman, Q. A.; Meggiolaro, D.; Dang, Z.; De Angelis, F.; Manna, L. Fluorescent Alloy CsPb_xMn_{1-x}I₃ Perovskite Nanocrystals with High Structural and Optical Stability. *ACS Energy Lett.* **2017**, 2 (9), 2183–2186.
- (23) Shen, X.; Zhang, Y.; Kershaw, S. V.; Li, T.; Wang, C.; Zhang, X.; Wang, W.; Li, D.; Wang, Y.; Lu, M.; Zhang, L.; Sun, C.; Zhao, D.; Qin, G.; Bai, X.; Yu, W. W.; Rogach, A. L. Zn-Alloyed CsPbI₃ Nanocrystals for Highly Efficient Perovskite Light-Emitting Devices. *Nano Lett.* **2019**, 19 (3), 1552–1559.
- (24) Imran, M.; Ramade, J.; Di Stasio, F.; De Franco, M.; Buha, J.; Van Aert, S.; Goldoni, L.; Lauciello, S.; Prato, M.; Infante, I.; Bals, S.; Manna, L. Alloy CsCd_xPb_{1-x}Br₃ Perovskite Nanocrystals: The Role of Surface Passivation in Preserving Composition and Blue Emission. *Chem. Mater.* **2020**, 32 (24), 10641–10652.

- (25) Paul, S.; Bladt, E.; Richter, A. F.; Döblinger, M.; Tong, Y.; Huang, H.; Dey, A.; Bals, S.; Debnath, T.; Polavarapu, L.; Feldmann, J. Manganese-Doping-Induced Quantum Confinement within Host Perovskite Nanocrystals through Ruddlesden–Popper Defects. *Angew. Chem. Int. Ed.* **2020**, 59 (17), 6794–6799.
- (26) Yang, C.-Q.; Yin, Z.-W.; Li, W.; Cui, W.-J.; Zhou, X.-G.; Wang, L.-D.; Zhi, R.; Xu, Y.-Y.; Tao, Z.-W.; Sang, X.; Cheng, Y.-B.; Van Tendeloo, G.; Hu, Z.-Y.; Su, B.-L. Atomically Deciphering the Phase Segregation in Mixed Halide Perovskite. *Adv. Funct. Mater.* **2024**, 34 (30), 2400569.
- (27) Yuan, B.; Yu, Y. High-Resolution Transmission Electron Microscopy of Beam-Sensitive Halide Perovskites. *Chem* **2022**, 8 (2), 327–339.
- (28) Teunissen, J. L.; Braeckevelt, T.; Skvortsova, I.; Guo, J.; Pradhan, B.; Debroye, E.; Roeffaers, M. B. J.; Hofkens, J.; Van Aert, S.; Bals, S.; Rogge, S. M. J.; Van Speybroeck, V. Additivity of Atomic Strain Fields as a Tool to Strain-Engineering Phase-Stabilized CsPbI₃ Perovskites. *J. Phys. Chem. C* **2023**, 127 (48), 23400–23411.
- (29) Shannon, R. D.; Prewitt, C. T. Effective Ionic Radii in Oxides and Fluorides. *Acta Crystallogr. Sect. B* **1969**, 25 (5), 925–946.
- (30) Shannon, R. D. Revised Effective Ionic Radii and Systematic Studies of Interatomic Distances in Halides and Chalcogenides. *Acta Crystallogr. Sect. A* **1976**, 32 (5), 751–767.
- (31) Dang, Z.; Luo, Y.; Wang, X.-S.; Imran, M.; Gao, P. Electron-Beam-Induced Degradation of Halide-Perovskite-Related Semiconductor Nanomaterials. *Chin. Opt. Lett.* **2021**, 19 (3), 030002.

- (32) Rothmann, M. U.; Kim, J. S.; Borchert, J.; Lohmann, K. B.; O'Leary, C. M.; Sheader, A. A.; Clark, L.; Snaith, H. J.; Johnston, M. B.; Nellist, P. D.; Herz, L. M. Atomic-Scale Microstructure of Metal Halide Perovskite. *Science* **2020**, 370 (6516), eabb5940.
- (33) Hu, J.; Bi, C.; Zhang, X.; Lu, Y.; Zhou, W.; Zheng, Z.; Tang, Y.; Lu, F.; Yao, Z.; Tian, B.; Wang, X.; Selvakumar, K.; Tian, J.; Sui, M. Yellow-Light Emitted Single Halide CsPbI₃ Nanowire. *Appl. Mater. Today* **2022**, 29, 101592.
- (34) Yin, Y.; Cheng, H.; Tian, W.; Wang, M.; Yin, Z.; Jin, S.; Bian, J. Self-Assembled δ-CsPbI₃ Nanowires for Stable White Light Emission. *ACS Appl. Nano Mater.* **2022**, 5 (12), 18879–18884.
- (35) Nellist, P. D. Scanning Transmission Electron Microscopy. In Science of Microscopy; Hawkes, P. W., Spence, J. C. H., Eds.; *Springer: New York* **2007**; 65–132.
- (36) De Backer, A.; van den Bos, K. H. W.; Van den Broek, W.; Sijbers, J.; Van Aert, S. StatSTEM: An Efficient Approach for Accurate and Precise Model-Based Quantification of Atomic Resolution Electron Microscopy Images. *Ultramicroscopy* **2016**, 171, 104–116.
- (37) Yu, Y.; Zhang, D.; Yang, P. Ruddlesden–Popper Phase in Two-Dimensional Inorganic Halide Perovskites: A Plausible Model and the Supporting Observations. *Nano Lett.* **2017**, 17 (9), 5489–5494.
- (38) Akkerman, Q. A.; Bladt, E.; Petralanda, U.; Dang, Z.; Sartori, E.; Baranov, D.; Abdelhady, A. L.; Infante, I.; Bals, S.; Manna, L. Fully Inorganic Ruddlesden–Popper Double Cl–I and Triple Cl–Br–I Lead Halide Perovskite Nanocrystals. *Chem. Mater.* **2019**, 31 (6), 2182–2190.
- (39) Thind, A. S.; Luo, G.; Hachtel, J. A.; Morrell, M. V.; Cho, S. B.; Borisevich, A. Y.; Idrobo, J.-C.; Xing, Y.; Mishra, R. Atomic Structure and Electrical Activity of Grain Boundaries and

Ruddlesden-Popper Faults in Cesium Lead Bromide Perovskite. *Adv. Mater.* **2019**, 31 (4), 1805047.

- (40) Li, J.; Yu, Q.; He, Y.; Stoumpos, C. C.; Niu, G.; Trimarchi, G. G.; Guo, H.; Dong, G.; Wang, D.; Wang, L.; Kanatzidis, M. G. Cs₂PbI₂Cl₂, All-Inorganic Two-Dimensional Ruddlesden–Popper Mixed Halide Perovskite with Optoelectronic Response. *J. Am. Chem. Soc.* **2018**, 140 (35), 11085–11090.
- (41) Lee, A.; Park, J. H.; Kim, H.; Jeong, H. Y.; Lee, J. H.; Song, M. H. Blue Perovskite Nanocrystal Light-Emitting Diodes: Overcoming Ruddlesden-Popper Fault-Induced Nonradiative Recombination via Post-Halide Exchange. *Small* **2022**, 18 (52), 2205011.
- (42) Mao, L.; Ke, W.; Pedesseau, L.; Wu, Y.; Katan, C.; Even, J.; Wasielewski, M. R.; Stoumpos, C.C.; Kanatzidis, M. G. Hybrid Dion-Jacobson 2D Lead Iodide perovskite. *J. Am. Chem. Soc.* **2018**, 140 (10), 3775-3783.
- (43) Abakumov, A. M.; Hadermann, J.; Batuk, M.; D'Hondt, H.; Tyablikov, O. A.; Rozova, M. G.; Pokholok, K. V.; Filimonov, D. S.; Sheptyakov, D. V.; Tsirlin, A. A.; Niermann, D.; Hemberger, J.; Van Tendeloo, G.; Antipov, E. V. Slicing the Perovskite Structure with Crystallographic Shear Planes: The A_nB_nO_{3n-2} Homologous Series. *Inorg. Chem.* **2010**, 49 (20), 9508–9516.
- (44) Nikolaev, I. V.; D'Hondt, H.; Abakumov, A. M.; Hadermann, J.; Balagurov, A. M.; Bobrikov, I. A.; Sheptyakov, D. V.; Pomjakushin, V. Yu.; Pokholok, K. V.; Filimonov, D. S.; Van Tendeloo, G.; Antipov, E. V. Crystal Structure, Phase Transition, and Magnetic Ordering in Perovskite-like Pb_{2-x}Ba_xFe₂O₅ Solid Solutions. *Phys. Rev. B* **2008**, 78 (2), 024426.

- (45) Wang, P.; Bleloch, A. L.; Yan, L.; Niu, H. J.; Chalker, P. R.; Rosseinsky, M. J.; Goodhew, P. J. Aberration Corrected STEM of Defects in Epitaxial N=4 Ruddlesden-Popper Phase Ca_{n+1}Mn_nO_{3n+1}. *J. Phys. Conf. Ser.* **2008**, 126 (1), 012050.
- (46) Li, J.; Chen, J.; Xu, L.; Liu, S.; Lan, S.; Li, X.; Song, J. A Zinc Non-Halide Dopant Strategy Enables Efficient Perovskite CsPbI₃ Quantum Dot-Based Light-Emitting Diodes. *Mater. Chem. Front.* **2020**, 4 (5), 1444–1453.
- (47) Torma, A. J.; Li, W.; Zhang, H.; Tu, Q.; Klepov, V. V.; Brennan, M. C.; McCleese, C. L.; Krzyaniak, M. D.; Wasielewski, M. R.; Katan, C.; Even, J.; Holt, M. V.; Grusenmeyer, T. A.; Jiang, J.; Pachter, R.; Kanatzidis, M. G.; Blancon, J.-C.; Mohite, A. D. Interstitial Nature of Mn²⁺ Doping in 2D Perovskites. *ACS Nano* **2021**, 15 (12), 20550–20561.
- (48) Batatia, I.; Kovács, D. P.; Simm, G. N. C.; Ortner, C.; Csányi, G. M. MACE: Higher-Order Equivariant Message Passing Neural Networks for Fast and Accurate Force Fields. *arXiv* [stat.ML], **2023**, arXiv:2206.07697.
- (49) Hutter, J.; Iannuzzi, M.; Schiffmann, F.; Vandevondele, J. Cp2k: Atomistic Simulations of Condensed Matter Systems. *Wiley Interdiscip. Rev. Comput. Mol. Sci.* **2014**, 4 (1), 15–25.
- (50) Vandenhaute, S.; Cools-Ceuppens, M.; DeKeyser, S.; Verstraelen, T.; Van Speybroeck, V. Machine Learning Potentials for Metal-Organic Frameworks Using an Incremental Learning Approach. *NPJ Comput. Mater.* **2023**, 9 (1), 1–8.
- (51) Lobato, I.; Van Aert, S.; Verbeeck, J. Progress and New Advances in Simulating Electron Microscopy Datasets Using MULTEM. *Ultramicroscopy* **2016**, 168, 17–27.

- (52) Steele, J. A.; Braeckevelt, T.; Prakasam, V.; Degutis, G.; Yuan, H.; Jin, H.; Solano, E.; Puech, P.; Basak, S.; Pintor-Monroy, M. I.; Van Gorp, H.; Fleury, G.; Yang, R. X.; Lin, Z.; Huang, H.; Debroye, E.; Chernyshov, D.; Chen, B.; Wei, M.; Hou, Y.; Gehlhaar, R.; Genoe, J.; De Feyter, S.; Rogge, S. M. J.; Walsh, A.; Sargent, E. H.; Yang, P.; Hofkens, J.; Van Speybroeck, V.; Roeffaers, M. B. J. An Embedded Interfacial Network Stabilizes Inorganic CsPbI₃ Perovskite Thin Films. *Nat. Commun.* **2022**, 13 (1), 7513.
- (53) Chen, G.-Y.; Guo, Z.-D.; Gong, X.-G.; Yin, W.-J. Kinetic Pathway of γ-to-δ Phase Transition in CsPbI₃. *Chem* **2022**, 8 (11), 3120–3129.
- (54) Pradhan, B.; Mushtaq, A.; Roy, D.; Sain, S.; Das, B.; Ghorai, U. K.; Pal, S. K.; Acharya, S. Postsynthesis Spontaneous Coalescence of Mixed-Halide Perovskite Nanocubes into Phase-Stable Single-Crystalline Uniform Luminescent Nanowires. *J. Phys. Chem. Lett.* **2019**, 10 (8), 1805–1812.
- (55) Zhang, Y.; Siegler, T. D.; Thomas, C. J.; Abney, M. K.; Shah, T.; De Gorostiza, A.; Greene, R. M.; Korgel, B. A. A "Tips and Tricks" Practical Guide to the Synthesis of Metal Halide Perovskite Nanocrystals. *Chem. Mater.* **2020**, 32 (13), 5410–5423.
- (56) Verstraelen, T.; Vanduyfhuys, L.; Vandenbrande, S.; Rogge, S. Yaff, yet Another Force Field. http://molmod.ugent.be/software/. (accessed 2024-12-23).
- (57) Bussi, G.; Parrinello, M. Accurate Sampling Using Langevin Dynamics. *Phys. Rev. E* **2007**, 75 (5), 056707.
- (58) Feller, S. E.; Zhang, Y.; Pastor, R. W.; Brooks, B. R. Constant Pressure Molecular Dynamics Simulation: The Langevin Piston Method. *J. Chem. Phys.* **1995**, 103 (11), 4613–4621.

- (59) Grimme, S.; Antony, J.; Ehrlich, S.; Krieg, H. A Consistent and Accurate Ab Initio Parametrization of Density Functional Dispersion Correction (DFT-D) for the 94 Elements H-Pu. *J. Chem. Phys.* **2010**, 132 (15).
- (60) Perdew, J. P.; Burke, K.; Ernzerhof, M. Generalized Gradient Approximation Made Simple. *Phys. Rev. Lett.* **1996**, 77 (18), 3865.
- (61) Eastman, P.; Galvelis, R.; Peláez, R. P.; Abreu, C. R. A.; Farr, S. E.; Gallicchio, E.; Gorenko, A.; Henry, M. M.; Hu, F.; Huang, J.; Krämer, A.; Michel, J.; Mitchell, J. A.; Pande, V. S.; Rodrigues, J. P.; Rodriguez-Guerra, J.; Simmonett, A. C.; Singh, S.; Swails, J.; Turner, P.; Wang, Y.; Zhang, I.; Chodera, J. D.; De Fabritiis, G.; Markland, T. E. OpenMM 8: Molecular Dynamics Simulation with Machine Learning Potentials. *J. Phys. Chem. B* **2024**, 128 (1), 109–116.

Supporting information

Increasing the phase stability of CsPbI₃ nanocrystals by Zn²⁺ and Cd²⁺ addition: synergy of transmission electron microscopy and molecular dynamics

Irina Skvortsova¹‡, Tom Braeckevelt^{2,3}‡, Annick De Backer¹, Nadine Schrenker¹, Bapi Pradhan³, Johan Hofkens³, Sandra Van Aert¹, Veronique Van Speybroeck², Sara Bals^{1*}

¹ Electron microscopy for materials science (EMAT) and NANOlab Center of Excellence, University of Antwerp, Groenenborgerlaan 171, 2020 Antwerp, Belgium

² Center for molecular modeling (CMM), Ghent University, Technologiepark 46, 9052 Zwijnaarde, Belgium

³ Department of Chemistry, KU Leuven, Celestijnenlaan 200F, 3001 Leuven, Belgium

‡These authors contribute equally

*Corresponding author: sara.bals@uantwerpen.be

Table of content

Supplementary Figures and Tables:

Figure S1 Structural models of black and yellow CsPbI₃, RP Cs₂PbI₄

Figure S2 Phase analysis

Table S1 Quantitative analysis of the composition

Figure S3 EDX spectra for three CsPbI₃ samples

Figure S4 Demonstration of RP-like planar defects after NCs agglomeration

Figure S5 Probabilities analysis for the atoms belonging to either RP or perovskite phase close to the interfaces

Figure S6 Scheme about CsI layer variation in RP structure

Figure S7 EDX spectroscopy at high magnification

Table S2 Composition for RP and perovskite regions

Figure S8 Line profiles for simulated and experimental images of one-shift RP-like phase

Figure S9 Atomic coordinates plots for one-shift RP-like phase

Figure S10 Intercolumn distances calculated for the experimental images with RP-like regions

Figure S11 Explanation of the column compositions in RP-like phases

Figure S12 MD-averaged structures of the RP phases with dopants

Table S3 Stability of the RP structures with Cd in Cs or Pb position with different coordination number

Figure S13, Figure S14 RP-perovskite interfaces

Figure S15 Schematic representation of the RP phases with the corresponding in- and out-of-plane shifts

Coordination environment of Zn: energetical aspect

Table S4, Table S5 Energy differences for Zn-substituted two-shift RP structures with different coordination number

HAADF-STEM image simulations

Table S6 Settings used for the HAADF-STEM images simulation

Structure generation

MD simulations

Figure S16 Time evolution of energy and temperature in an MD simulation

MLP development via active learning

Table S7 Settings of the applied MACE architecture to train the MLPs

Comparison of the universal and specific machine learning potentials

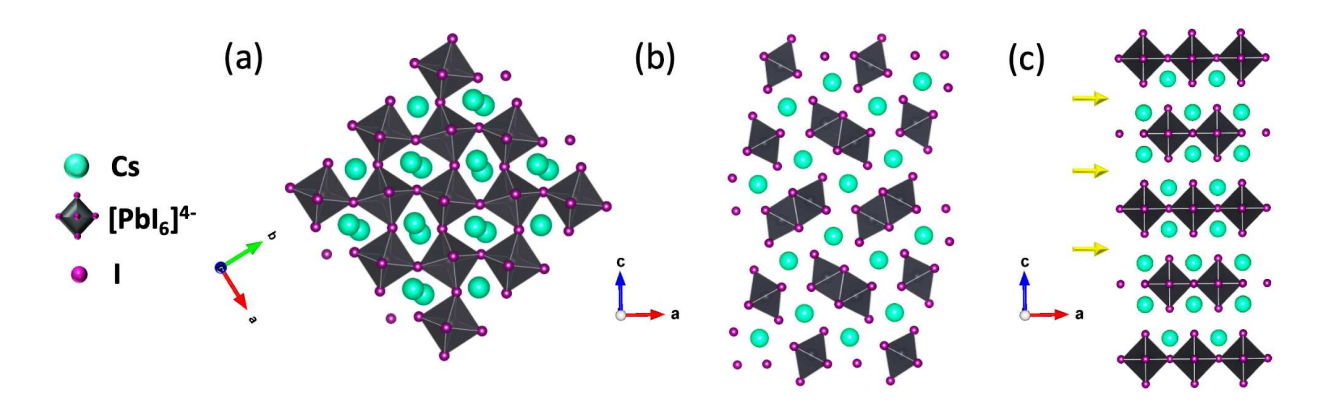


Figure S1. Structure models of (a) orthorhombic γ -, (b) orthorhombic δ- CsPbI₃ phases and n=1 Ruddlesden-Popper structures (c). Yellow arrows for (c) highlight extra CsI layers inbetween perovskite layers.

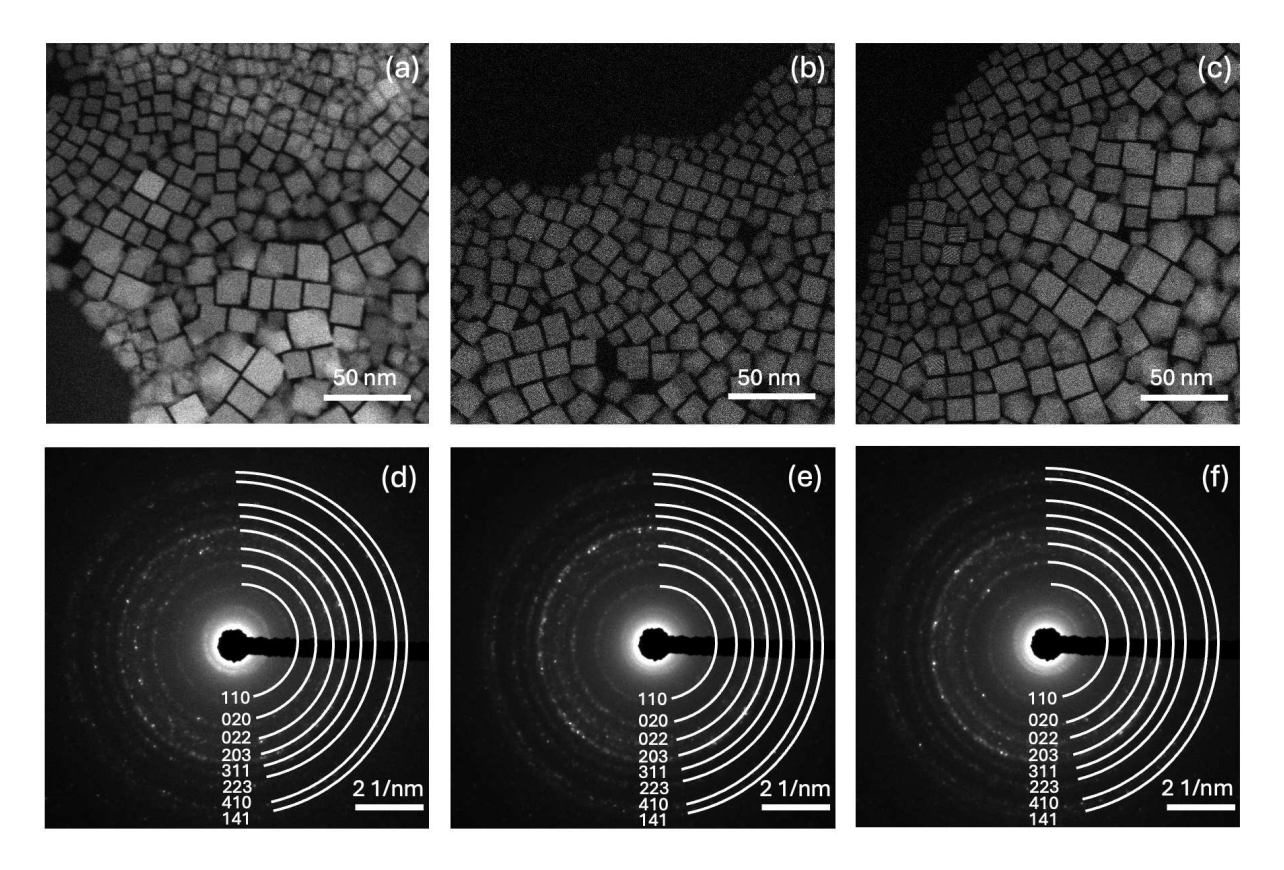


Figure S2. HAADF-STEM overview images of (a) undoped CsPbI₃, (b) Zn-doped CsPbI₃ and (c) Cd-doped CsPbI₃ NCs. The corresponding SAED diffraction patterns are presented in (d, e, f) indexed in the orthorhombic crystal system (*Pnma*).

Table S1. EDX quantitative elemental analysis for the unmodified, Cd-modified and Zn-modified CsPbI₃ nanocrystals.

Sample	Cs, at.%	Pb, at.%	I, at.%	Zn/Cd, at.%
CsPbI ₃	20.92±2.1	19.77±2.4	61.31±1.5	-
Cd-modified CsPbI ₃	21.87±1.7	18.39±1.1	59.85±1.3	2.51±0.8
Zn-modified CsPbI ₃	18.70±1.2	21.35±1.6	57.90±2.4	2.05±0.5

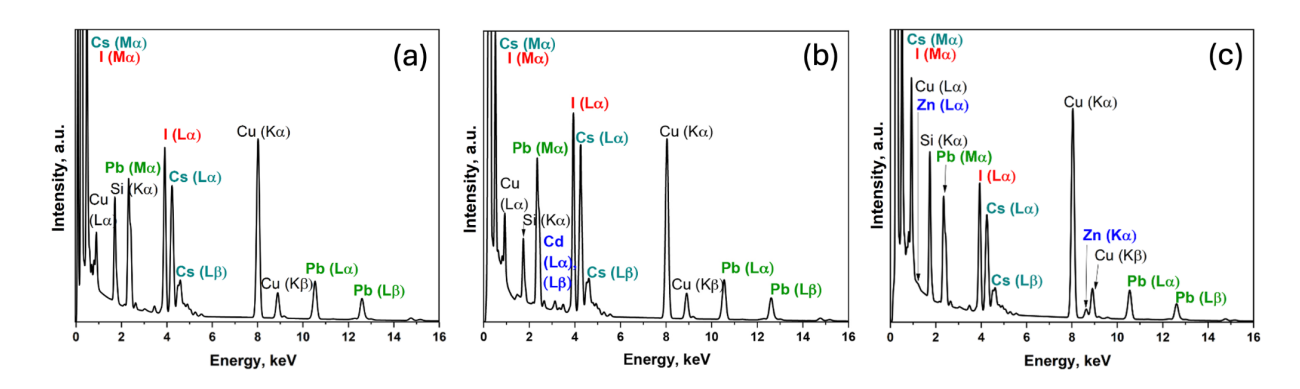


Figure S3. EDX spectra recorded for (a) unmodified, (b) Cd-modified and (c) Zn-modified CsPbI₃ nanocrystals.

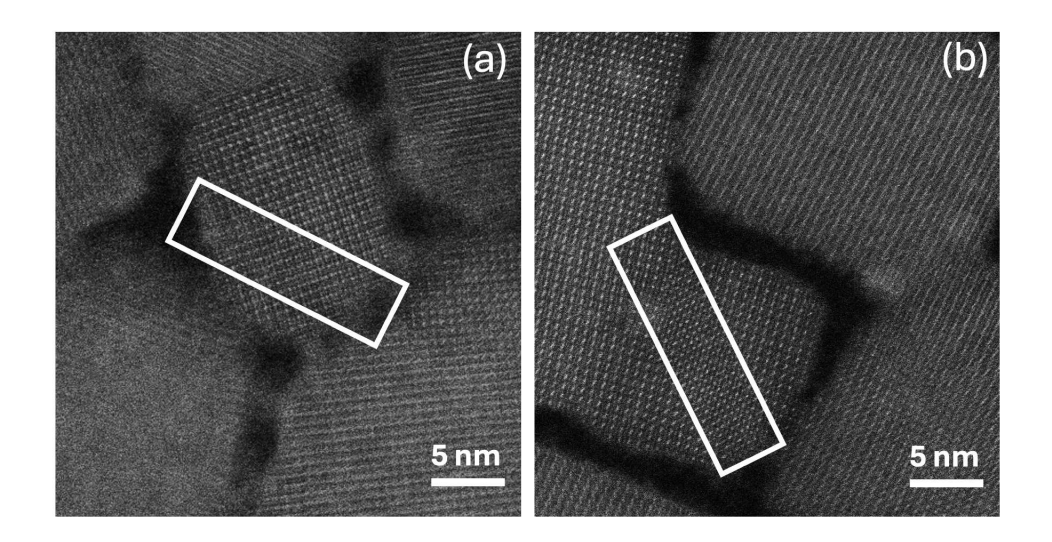


Figure S4. HAADF-STEM images of (a) Cd-doped and (b) Zn-doped CsPbI₃ NCs containing planar defects (highlighted by white frames) after exposing them to air for 3 and 5 days respectively.

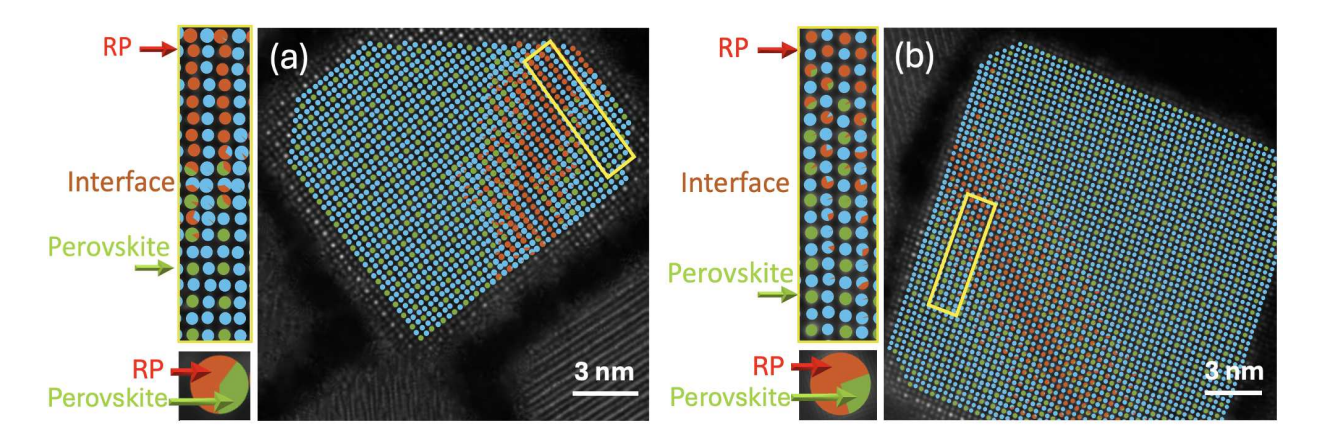


Figure S5. Zoomed-in analysis of RP/perovskite interface for Cd-modified and Zn-modified samples (a, b) where round markers for columns at the interface depicts the probability of their correspondence to either the perovskite (green) or RP (red) phases as identified according to the analyzed integrated intensities. Low intensity columns corresponding to Cs, I or Cs+I columns are indicated in blue color.

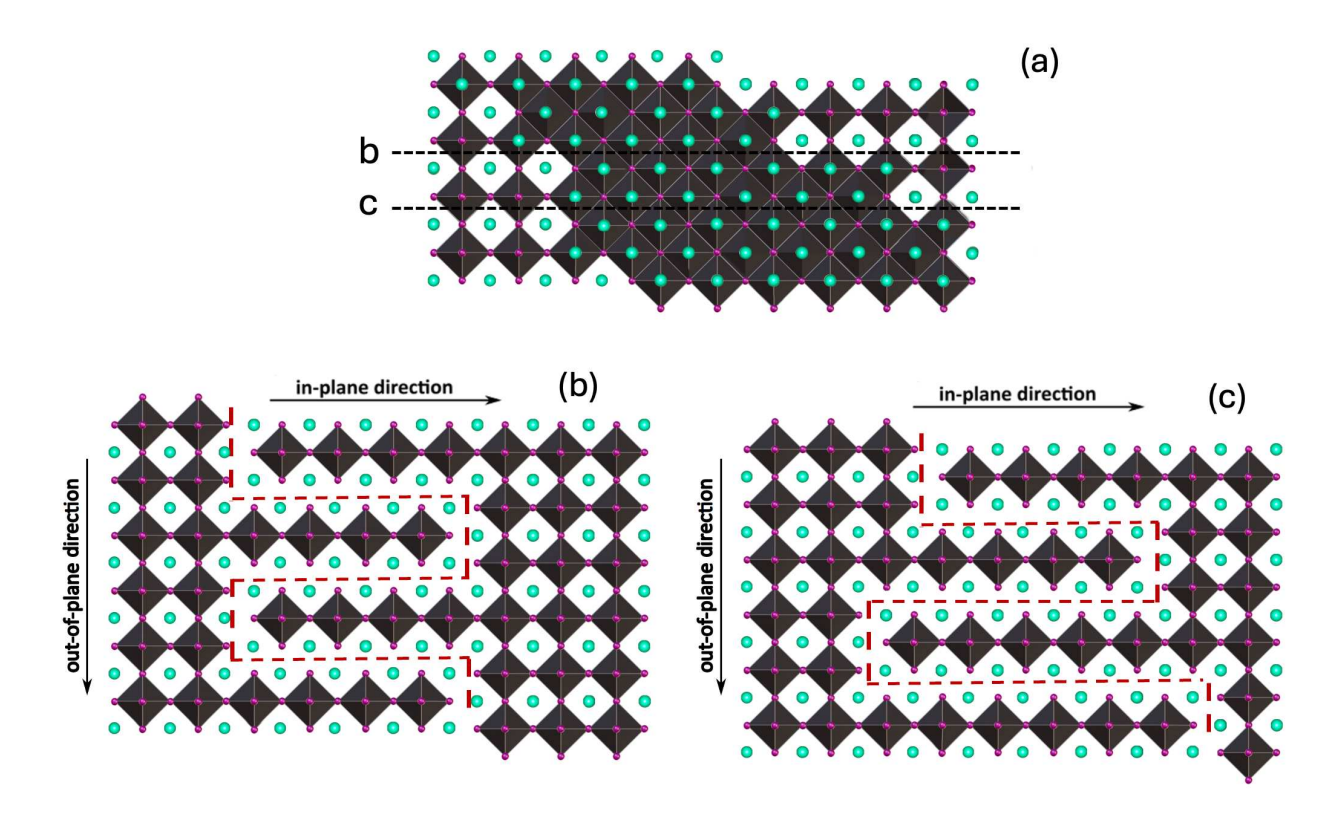


Figure S6. Schematic depiction of the two-shift 001-RP phase in experimentally observed zone axis (a). The black dashed lines in (a) indicate the regions of the cross-sections for (b) and (c). Schematic depiction of the cross-sections of two-shift 001-RP phase with (b) and without (c) CsI layer length variation. The interface is traced by red dashed lines.

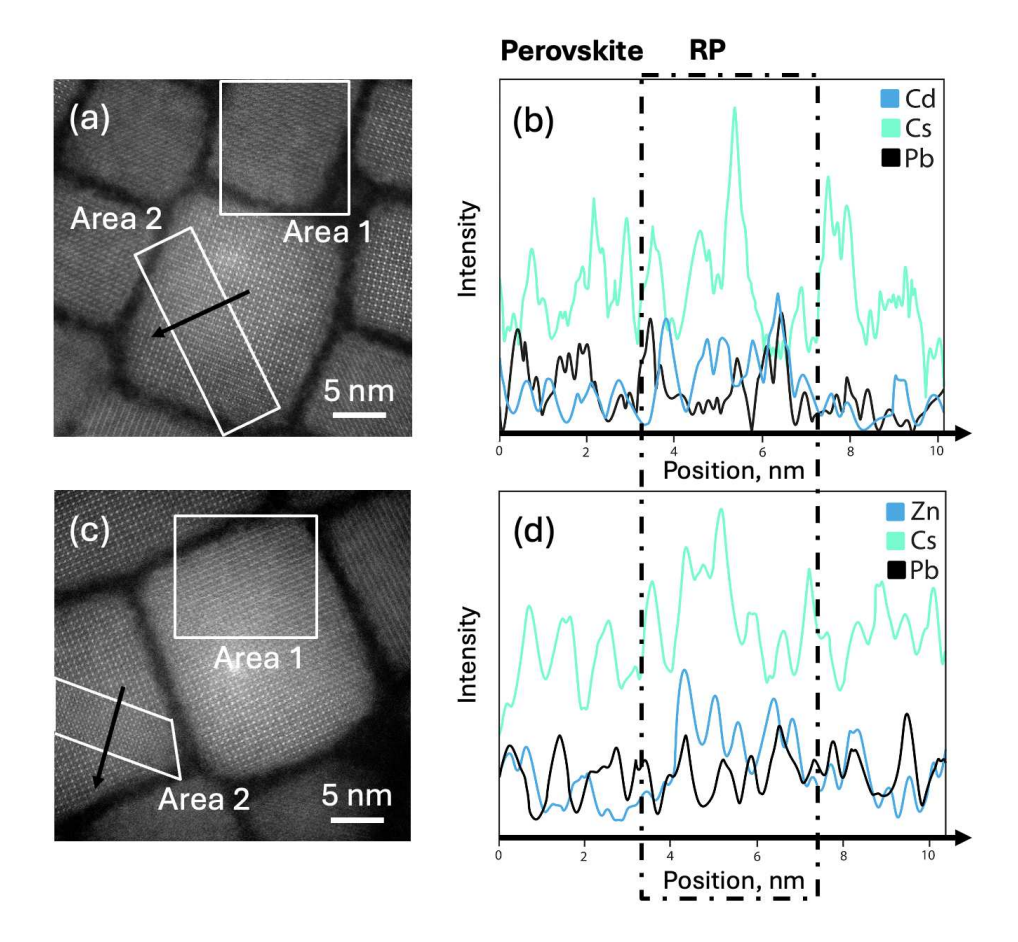


Figure S7. High-resolution HAADF-STEM images (a, c) with two areas indicated in white for composition quantification (**Table 1**): area 1-perovskite phase, area 2- RP-like region. Elemental profiles (b, d) of Cd/Zn, Cs and Pb obtained along the black arrow with integration over the regions of 10 nm width which includes planar defects (area 2) for Cd and Zn-containing CsPbI₃, respectively.

 $\label{eq:containing} \textbf{Table S2.} \ EDX \ quantitative \ elemental \ analysis \ for the \ undoped, Zn- \ and \ Cd-containing \ CsPbI_3$ NCs.

Sample	Area	Cs, at. %	Pb, at. %	I, at. %	Cd or Zn, at.
					%
Cd-	1	19.6±1.1	18.9±1.6	60.1±2.3	1.4±0.8
modified	(perovskite)				
CsPbI ₃	2 (RP-like	28.3±2.9	11.7±2.3	56.3±3.4	3.7±0.7
	region)				
Zn-	1	19.2±1.0	19.5±1.2	60.2±1.7	1.1±0.8
modified	(perovskite)				
CsPbI ₃	2 (RP	25.5±2.6	15.8±1.9	56.5±3.1	2.2±0.5
	region)				

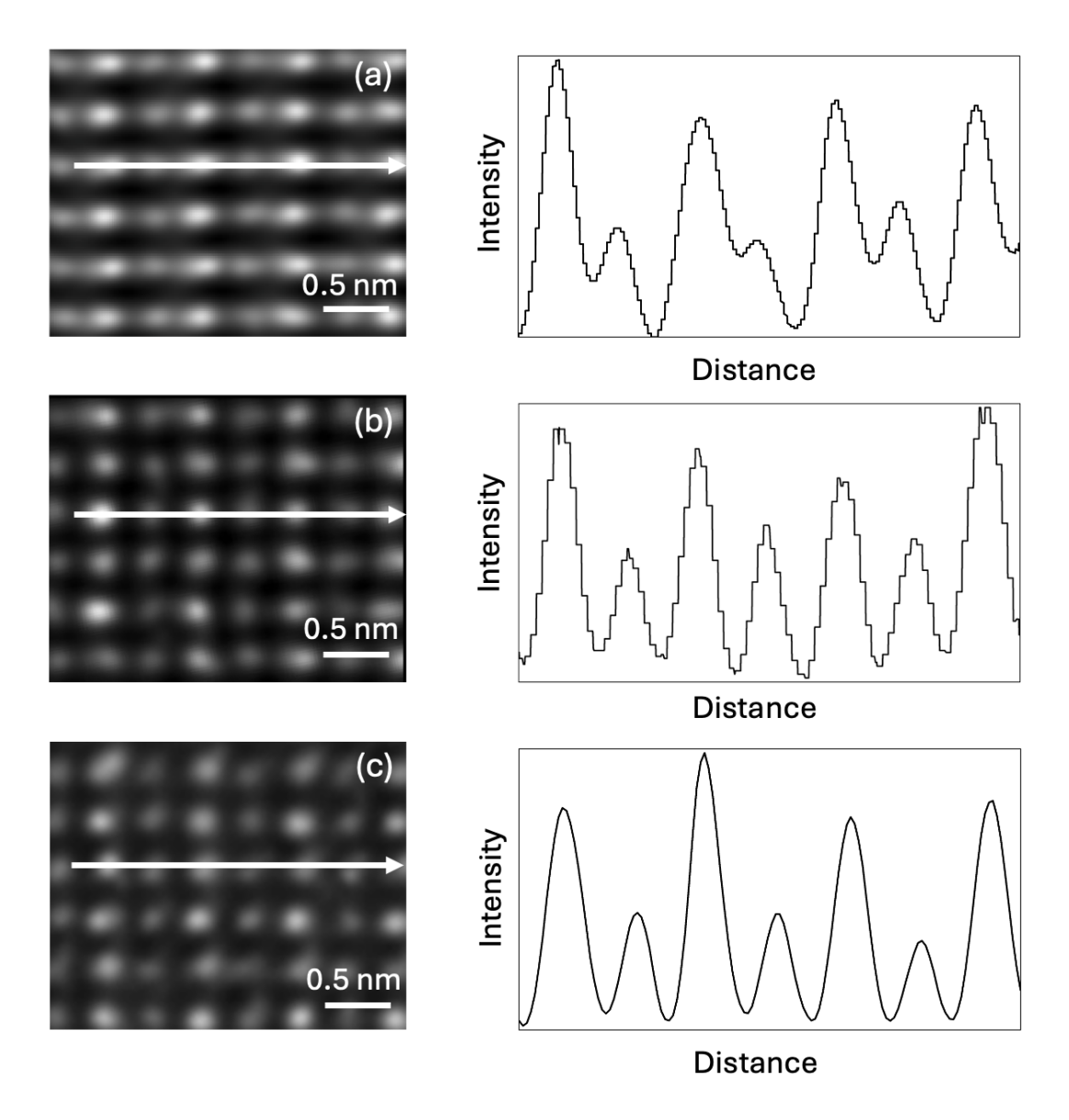


Figure S8. Line profiles plotted along the white arrow for simulated 001-one-shift RP phase (a), simulated 110-one-shift RP phase (b) and the Gaussian-filtered experimental image of the region with one-shift RP fault (c).

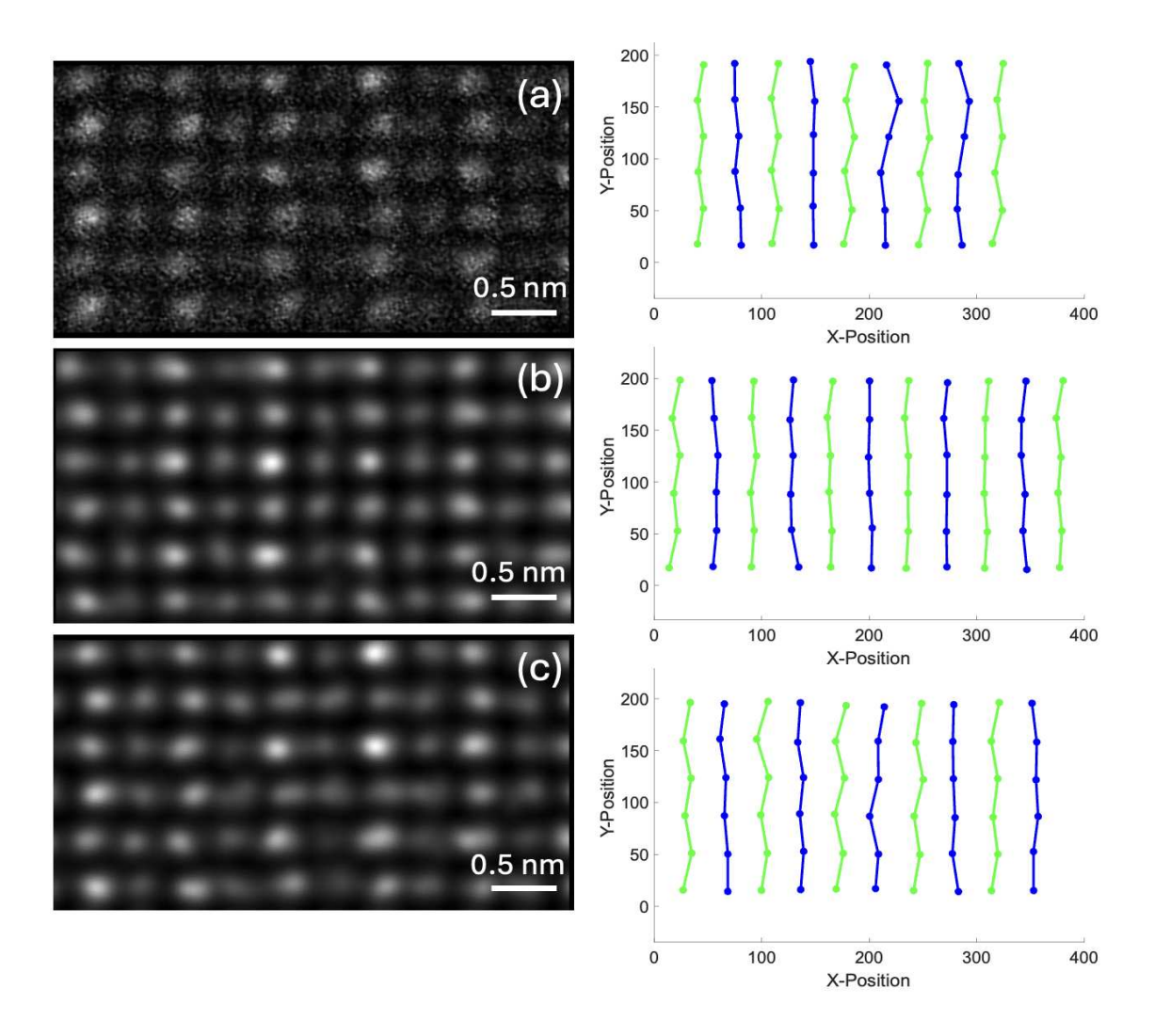


Figure S9. Atomic coordinates plot of Pb+I columns corresponding to the atomic positions in the experimental region with one-shift RP fault (a). Atomic coordinates plot of Pb+I columns corresponding to atomic positions in a simulated image of 110 one-shift RP phase (b) and Cd-containing 110 one-shift RP phase (c). Green color corresponds to Pb+I columns, while Cs+I columns are colored by blue. For the last structure, three of the 64 Pb²⁺ cations in the simulation cell are substituted by Cd²⁺.

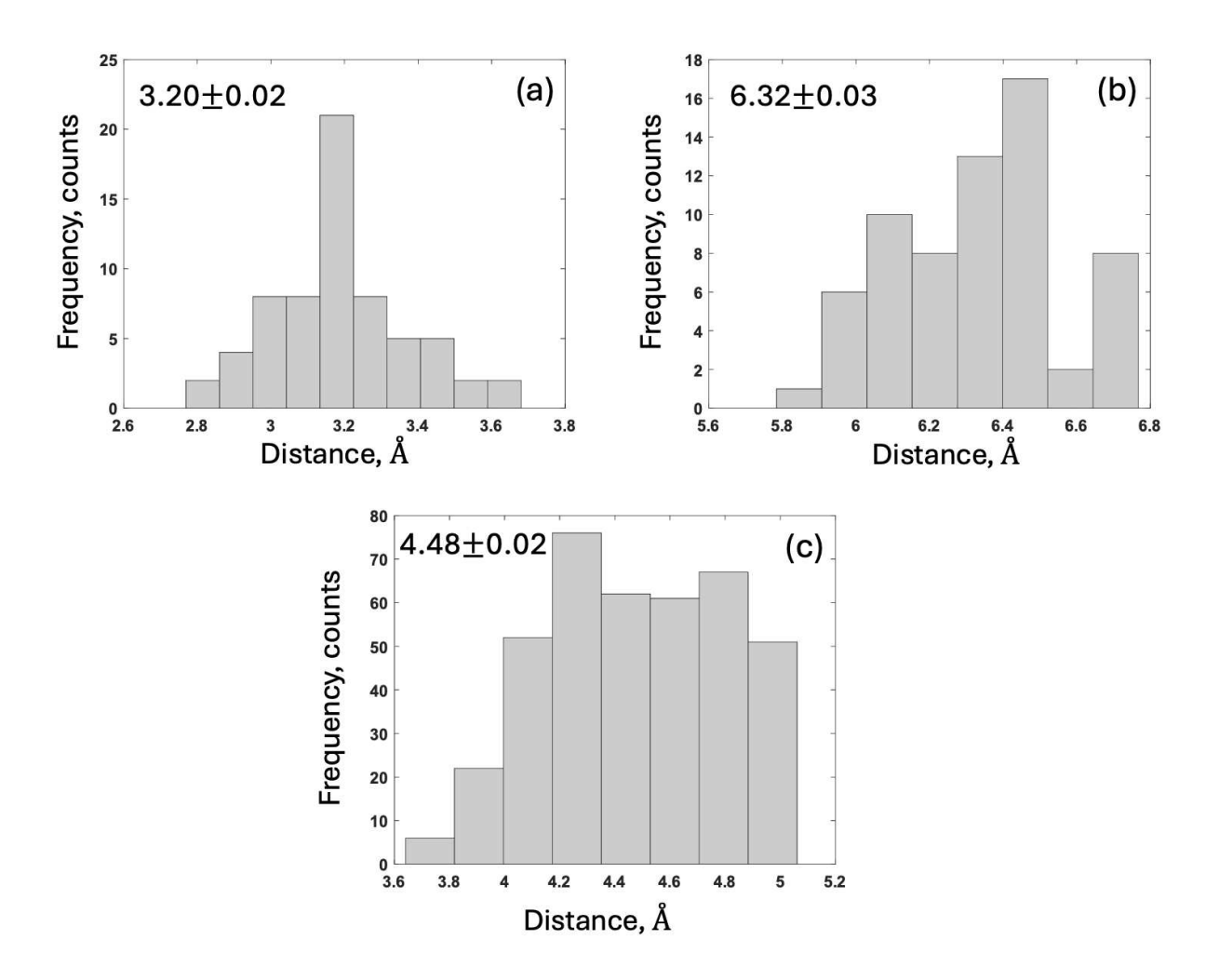


Figure S10. Histograms depicting the intercolumns distances distributions for experimental images of the regions with one-shift RP-like phase (a), (b) and two-shift RP-like phase (c).

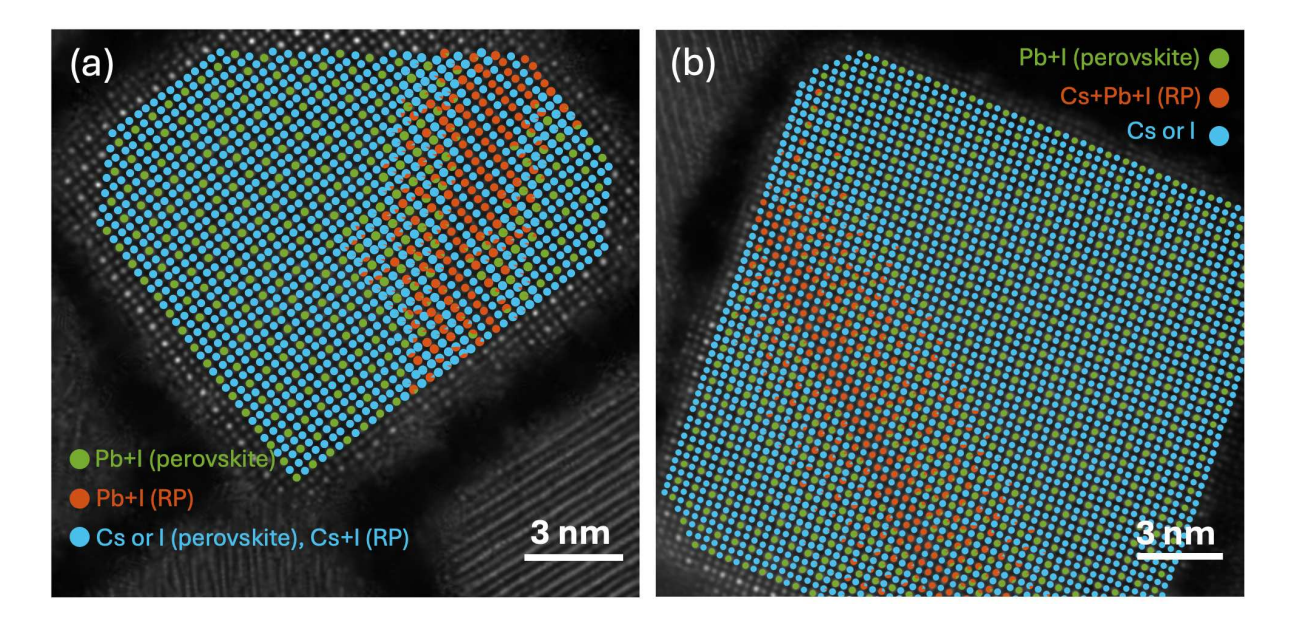


Figure S11. For one-shift RP phase (a), found for Cd-doped sample, the total intensities of the columns were found to be lower (red) in comparison to the perovskite Pb+I column (green). This matches with the crystal structure of the one-shift RP model where high-intensity columns include iodine-rich Pb+I, while for perovskite phase such columns contain an equivalent amount of these elements (Pb and I). There are also Cs+I columns (blue) in-between Pb+I columns (red) in this type of RP phase (a). The high-intensity columns (red) found in (b) the two-shift RP phase, Zn-doped sample include all types of atoms (Pb, I and Cs). The low-intensity atomic columns (blue) contain only I atoms in-between Cs+Pb+I columns (red) in two-shift RP phase.

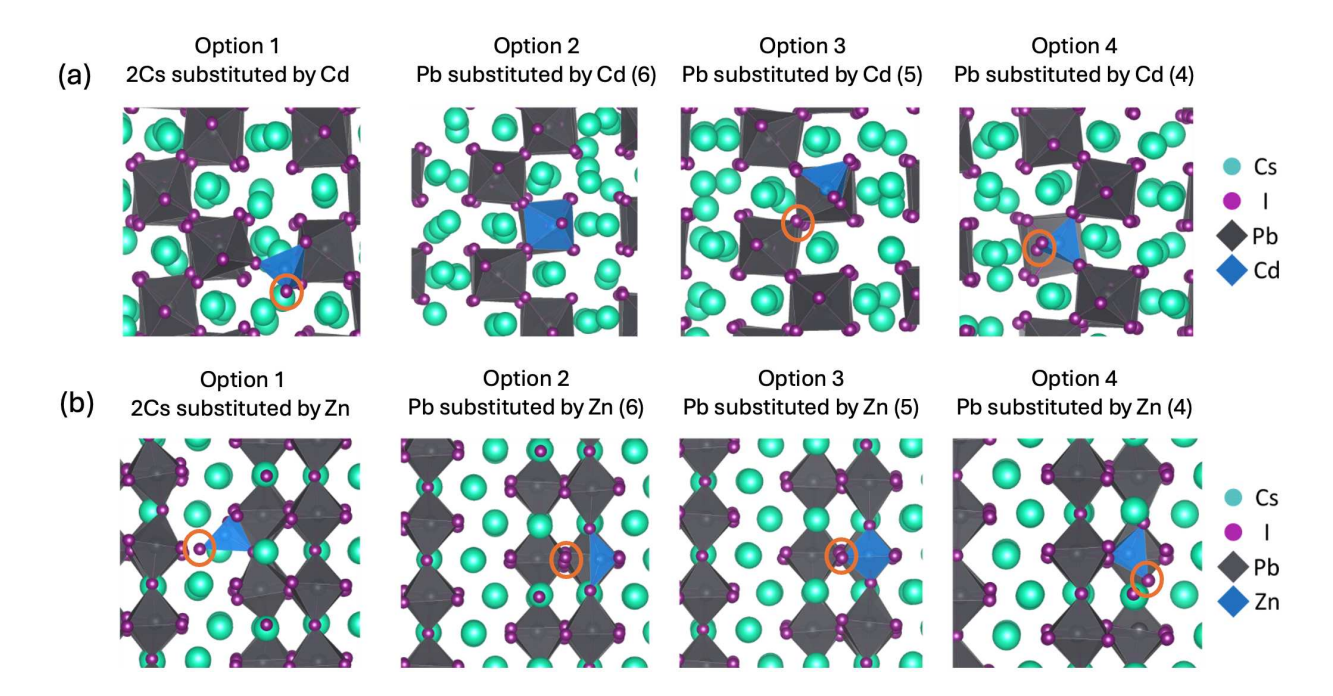


Figure S12. (a) Averaged structures from 380 ps MD simulations at 300 K and 0.1 MPa for the Cd-incorporated 110 one-shift RP phase. (b) Averaged structures from 180 ps MD simulations at 300 K and 0.1 MPa for the Zn-incorporated 110 two-shift RP phase. Orange circles indicate Pb–I bond breaking due to Zn or Cd incorporation. In all cases, 1 out of the 64 Pb²⁺ cations in the simulation cell is substituted.

Table S3. Fraction of MD simulations for which the 110-one-shift RP phase remained stable. For each Cd concentration, and substitution option, 5 MD simulations of 400 ps at 300 K and 0.1 MPa were performed.

		001 one-shift RP-like structures		110 one-shift RP-like structures			
Pure stru	ıcture	0%		0% 100%			
Cd per 64	formula	1	3	6	1	3	6
unit	S						
Cs substi	itution	0%	20%	40%	60%	60%	100%
Pb	6 I ⁻	0%	20%	0%	100%	100%	80%
substitution	5 I-	0%	20%	100%	100%	100%	100%
	4 I ⁻	40%	0%	0%	40%	100%	100%

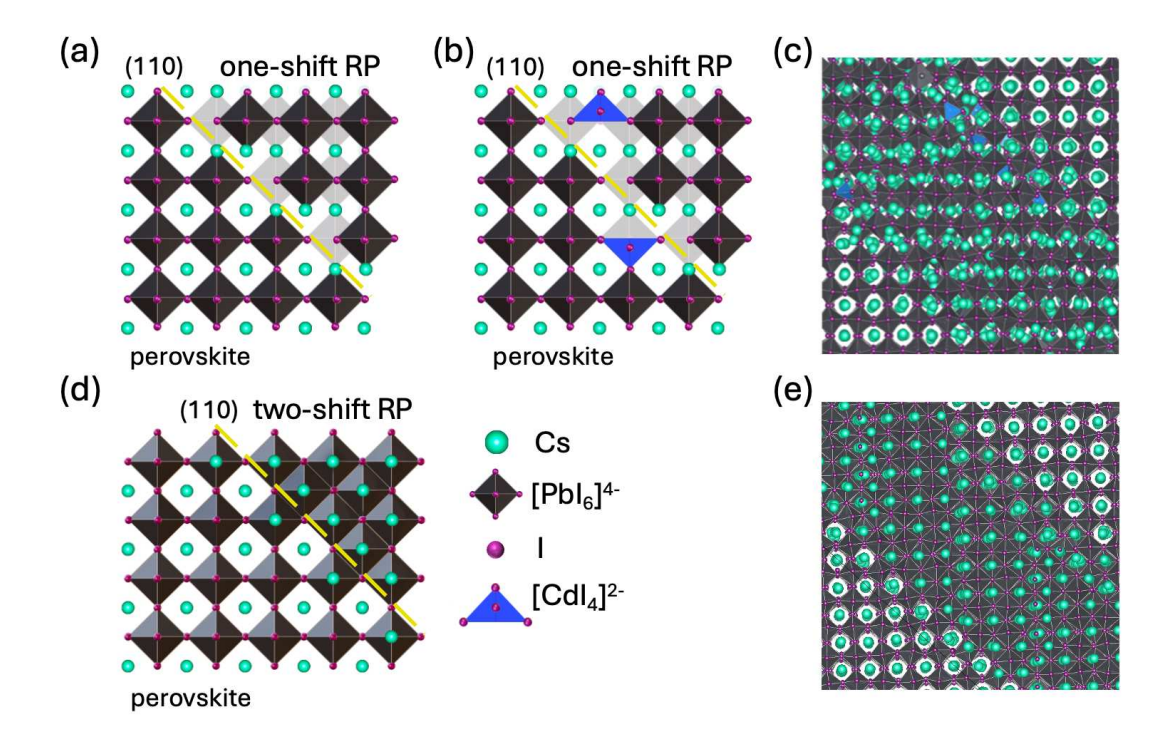


Figure S13. Schematic depiction of the interface between the perovskite and pure 110 one-shift (a) and 110 two-shift (d) RP-like phases as well as scheme of the interface (b) between the perovskite and Cd-incorporated 110 one-shift RP-like phase. Average structures of the Cd-incorporated interface between the perovskite and 110 one-shift RP-like phase (c) during 180 ps of MD simulation at 300 K and 0.1 MPa. We replaced one out of six [PbI₆]⁴⁻ octahedra (black) at the interface with [CdI₄]²⁻ tetrahedra (blue). Average structures of the interfaces between the perovskite and 110 two-shift RP-like phase (e) during 180 ps of MD simulation at 300 K and 0.1 MPa.

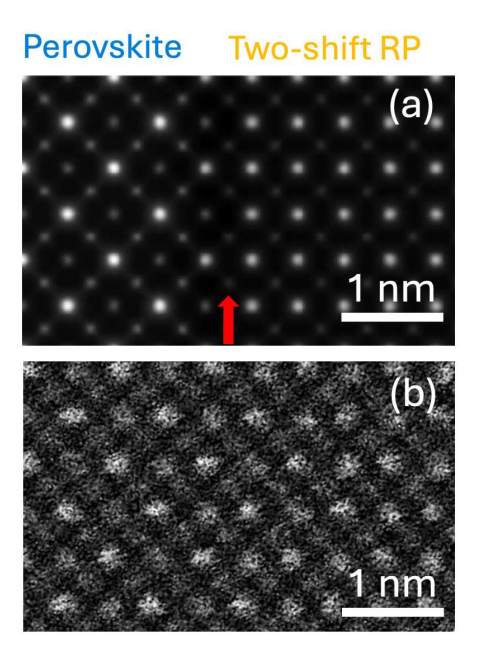


Figure S14. Interface of two-shift RP/perovskite. Comparison of images simulated with MULTEM (a) and experimental HAADF-STEM (b) images for the two-shift RP/perovskite interface. Red arrow points at the drastic change in the atomic column intensities since the simulated model does not take into account variation of the CsI layers lengths along the out-of-plane direction.

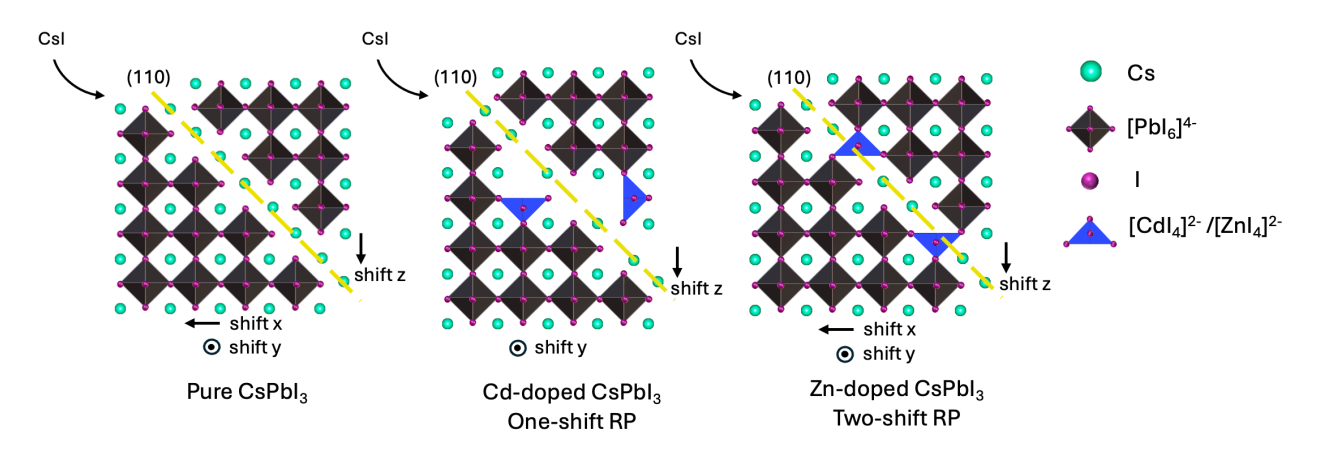


Figure S15. Schematic representation of the RP phases with the corresponding in- and out-of-plane shifts without any dopants and in a presence of Cd (4) in Pb position and Zn (4) in Pb positions. Due to different ionic radii of Zn^{2+} and Cd^{2+} the formation of the RP phase from the perovskite phase is triggered in a different manner.

Coordination environment of Zn: energetical aspect

To investigate the energetical aspect of the coordination environment of Zn in two-shift RP structure, the energy difference between the octahedral coordination and the 5- or 4-coordinated structures is compared for the substituted structures (i.e. with Zn incorporated) with the pure RP-structures. The absolute energy differences can not be interpreted quantitatively due to the stoichiometry difference between the different coordinated structures. Therefore, in Tables S4 and S5, the energy difference between the 5- or 4-coordination and 6-coordination for the substituted structures is subtracted from the energy difference for the pure structures for the 001- and 110-plane two-shift RP phases, respectively. This indicates whether Zn has a greater tendency for undercoordination than Pb.

The reported difference between the substituted and pure structures of the energy difference between 5- or 4-coordination and 6-coordination is depicted by the following equation:

$$\Delta^{Zn} \Delta_{coord} E = \Delta_{coord} E^{Zn} - \Delta_{coord} E^{Pb} = (E_{z-co}^{Zn} - E_{6-co}^{Zn}) - (E_{z-co}^{Pb} - E_{6-co}^{Pb})$$
(S1)

In the equation above, z refers to 5- or 4-coordination. The energies are determined by the average energies of 10 MD simulations of 180 ps at 300 K and 0.1 MPa. $\Delta^{Zn}\Delta_{coord}E$ can also be interpreted as the energy of the following reaction:

$$Cs_{2x-y}Pb_xI_{4x-y} + Cs_{2x}ZnPb_{x-1}I_{4x} \rightarrow Cs_{2x}Pb_xI_{4x} + Cs_{2x-y}ZnPb_{x-1}I_{4x-y}$$
 (S2)

In the reaction above, x determines the concentration of the substituent and was set to 64. Y is either 1 (referring to 5-coordination of the substituent or one Pb²⁺ cation) or 2 (referring to 4-coordination of substituent or one Pb²⁺ cation). The reaction describes the transfer of CsI pairs from the fully coordinated substituted structure to an undercoordinated pure structure.

Table S4. The energy difference per substituent for the 001-plane two-shift RP phase between the 5- or 4-coordination and 6-coordination for the substituted structures is subtracted from the energy difference for the pure structures, see Equation S1. The energies are determined by the average energies of 10 MD simulations of 180 ps at 300 K and 0.1 MPa. One out of 64 Pb²⁺ cations is substituted with Zn²⁺ and has its coordination changed to 5 or 4 I⁻ neighbors.

$\Delta^{Subst}\Delta_{coor}$	Zn	
	5-coord	-9.80
001 -plane	4-coord	-28.91

Table S5. The energy difference per substituent for the 110-plane two-shift RP phase between the 5- or 4-coordination and 6-coordination for the substituted structures is subtracted from the energy difference for the pure structures, see Equation S1. The energies are determined by the average energies of 10 MD simulations of 180 ps at 300 K and 0.1 MPa. One out of 64 Pb²⁺ cations is substituted with Zn²⁺ and has its coordination changed to 5 or 4 I⁻ neighbors.

$\Delta^{Subst}\Delta_{coor}$	Zn	
	5-coord	-31.98
110 -plane	4-coord	-49.52

For both 110 and 001-two-shift RP phase, it is more probable for Zn to change their octahedral coordination compared to Pb. This agrees with the fact that Zn^{2+} is too small to fit the octahedral space and therefore breaks bonds with I^- forming a tetrahedral coordination.

HAADF-STEM image simulations

Table S6. Details of the HAADF-STEM images simulations with the MULTEM tool¹.

Parameter	Value
Acceleration voltage	300 kV
Defocus	14.0312 Å
Spherical aberration	0.001 mm
Convergence angle	21 mrad
Inner detector angle	46 mrad
Outer detector angle	215 mrad
FWHM of the source image	1.0 Å
Root mean squared displacement Cs	0.2804 Å
Root mean squared displacement Pb	0.1764 Å
Root mean squared displacement I	0.2500 Å
Number of phonon configurations	30

Structure generation

The Pb substitutions for the one- and two-shift RP phases were performed by randomly selecting Pb²⁺ cations and replacing them with Zn²⁺ and Cd²⁺. If necessary, the substituted cation coordination was changed by randomly removing an I⁻ anion that was not bound to another Pb²⁺ cation and an Cs⁺ cation that was in the proximity of the I⁻ anion.

The Cs substitutions for the two-shift RP phases were performed by selecting two neighboring Cs⁺ cations. For the 110-plane RP phase, six different removals of two neighboring Cs⁺ cations lead to unique structures. The Zn²⁺ or Cd²⁺ cation was placed at one of the Cs⁺ positions.

The Cs substitutions for the one-shift RP phases were performed by randomly selecting two neighboring Cs^+ cations that are located in between two perovskite layers and placing the Zn^{2+}

or Cd²⁺ cations on one of the Cs⁺ positions. All substitutions were performed for a 336-atom supercell of the 001- or 110-plane RP phases, both for the one- and two-shift structures.

The interface structures were generated from scratch by creating a structure consisting of multiple shifted copies of a Cs₈PbI₆ building block. Each copy gets shifted with a vector that is, in each direction, a multiple of the Pb-Pb distance. The shifted perovskite layers at the interface and in the RP phase are created by automatically selecting certain copies that are translated with an extra shift. For the interfaces with a two-shift RP phase, these copies are additionally shifted in each direction with the Pb-I bond distance. For the interface with the 110-one-shift RP phase, a shift in one direction is not performed and in another doubled. The 001-one-shift RP phases can also be constructed via an additional shift in only two directions. However, this will lead to atoms of different elements that overlap. Via this method, a lot of atoms are overlapping because we do use a Cs₈PbI₆ building block instead of a CsPbI₃ building block. However, when selecting an appropriate additional shift, only two atoms with the same element are overlapping, and we can easily remove one of them.

To remove the tension created by nearby atoms at the interface for the 110 one-shift RP phase, Pb²⁺ cations were substituted by Cd²⁺, and their coordination was changed to four I⁻ anions instead of six. This was done by randomly selecting Pb²⁺ cations at the interface and substituting them with Cd²⁺ cations. Only Pb²⁺ cations coming from the RP phase were selected. All structures were generated by using a few input structures and Python scripts, which are available at https://doi.org/10.5281/zenodo.14600071. These structures were used as initial structures for the performed MD simulations and can also be found via this link.

MD simulations

Yaff was used to perform the NPT MD simulations². The force evaluations were performed with a machine learning potential (MLP) trained on density functional theory (DFT) energies and forces. The timestep was set to 2 fs, and all simulations were 200 or 400 ps long. The first

20 ps of each MD simulation was used as equilibration time. Time evolution of energy and temperature in an MD simulation is shown in Figure S16. The temperature was set to 300 K and controlled with a Langevin thermostat³ using a time constant of 100 fs. The pressure was set to 0.1 MPa and controlled with a Langevin barostat⁴ using a time constant of 1 ps. The complete workflow containing all MD simulations and post-analysis Python scripts is available at https://doi.org/10.5281/zenodo.14600071. Only the assessment of the stability of the one-shift RP structures for a specific MD simulation was performed manually.

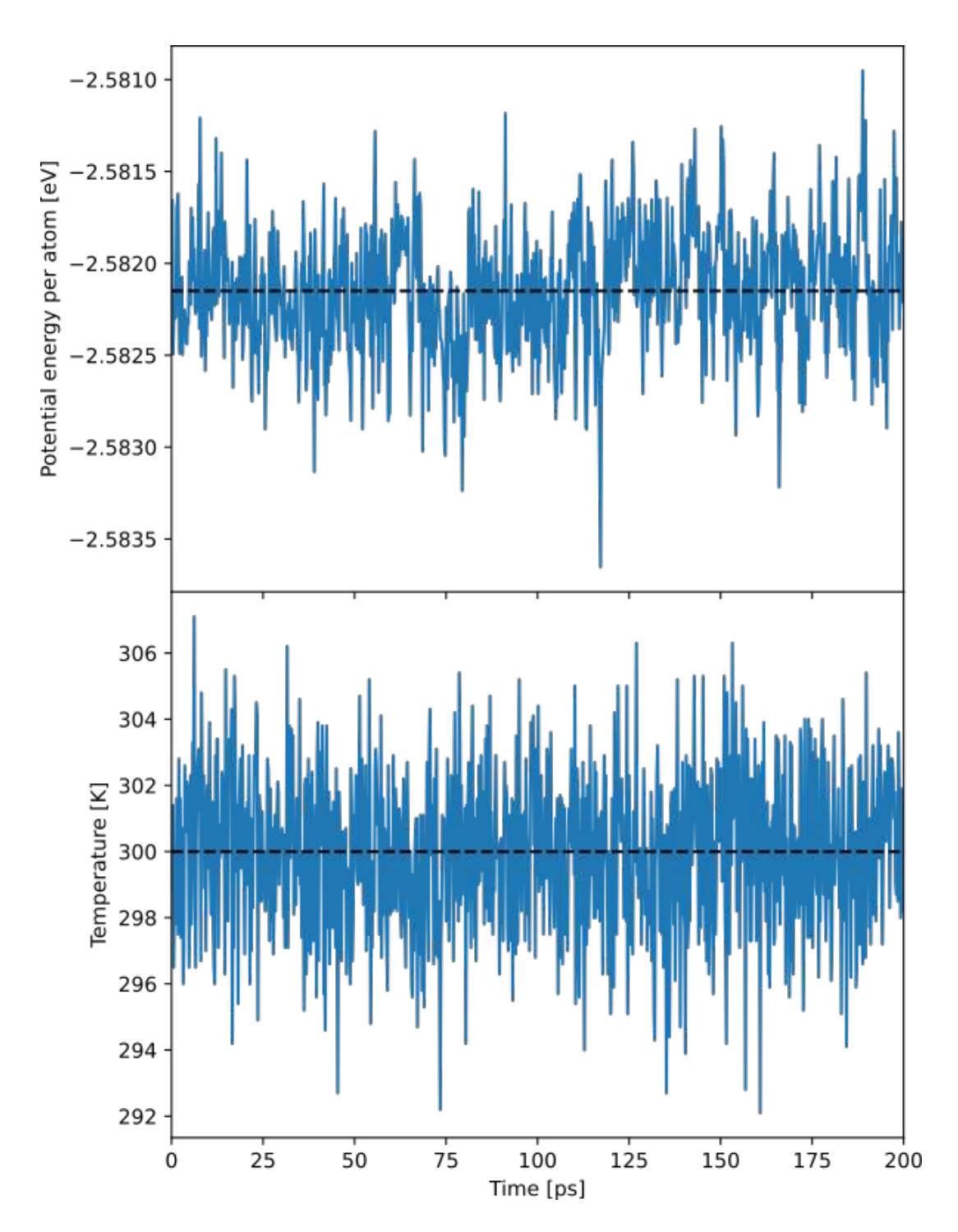


Figure S16. Potential energy per atom and temperature as a function of time for the NPT MD simulation at 300 K and 0.1 MPa of the structure corresponding to the 110 two-shift RP phase combined with the perovskite phase which was further used for the image simulation (Figure 5 (c)). The average structure was obtained from the trajectory between 20 and 200 ps. Dashed lines serve as a visual guide, indicating the average energy and temperature.

MLP training via active learning

Psiflow version 3.0.2⁵ was used to train the MLP via an active learning loop. Each iteration occurs in three steps. First, the ab initio energy and forces are calculated for an initial dataset of structures. Second, a new MLP is trained on the generated ab initio data set. Third, short MD simulations are performed with the new MLP to generate new set of input structures and expand the dataset via the active learning loop. These structures are then used in the following iteration, such that more ab initio energies and forces are added to the data set.

The set of structures discussed above (see Structure generation) can be used as an initial data set to perform ab initio calculations on and consequently train an initial MLP. However, the generated structures are artificial, and multiple picoseconds of equilibration time would be necessary before the relevant region of the phase space is sampled. Therefore, we use the MACE-MP-0⁶ universal MLP to equilibrate the structures for 200 or 400 ps. More information about this universal MLP is provided in the next section. The interface structures that were larger than 1200 atoms were not included in the initial set of structures because the ab initio calculations would not be feasible. The generated and equilibrated one-shift RP structures were both included in the initial data set. The initial data set contains 160 structures and can be found via https://doi.org/10.5281/zenodo.14600071. For every structure in the data set, the positions were randomly perturbed with 0.1 Å and the cell vectors with 0.05 Å before calculating the ab initio energy and forces.

The ab initio calculations were performed using DFT with the PBE-D3(BJ) exchange correlation (XC) functional^{7,8} as implemented in CP2K⁹. CP2K uses a combination of Gaussian and Plane Wave (GPW) basis sets. The GTH pseudopotentials and TZVP-MOLOPT-PBE-GTH basis sets were applied to all atoms^{10,11}. The cut-off and relative cut-off energies were set to 400 and 40 Ry, respectively. Due to the large simulation cells of the input structures, all calculations were performed on the Γ-point.

The MACE architecture ¹² with a cut-off radius of 7 Å was used to train the MLP. A few default settings of the MACE architecture defined in Psiflow were changed and are reported in Table S7. All MD simulations of the active learning loop were 4 ps long with a timestep of 2 fs. The pressure was set to 0.1 MPa and was controlled via a flexible Monte Carlo barostat¹³. The temperature was controlled at a specific value via Langevin dynamics¹⁴. For the first iteration of the active learning loop, the temperature of the MD simulation was set to 200 K. Up to the fifth iteration, the temperature of the MD simulation increased exponentially to 600 K. After the fifth iteration, the temperature was set to 600 K. Psiflow utilizes OpenMM¹⁵ to perform the NPT MD simulations during active learning. The complete overview of the CP2K, MACE, openMM, and psiflow settings can be found in the psiflow input files available at https://doi.org/10.5281/zenodo.14600071.

Table S7. Non-default settings of the applied MACE architecture to train the MLPs.

Setting	value
r_max	7.0
correlation	4
batch_size	2
max_num_epochs	120
patience	20
ema	True

The active learning loop was performed for 8 iterations, which generated training and validation data sets of 1411 and 157 structures, respectively. The final MLP trained for approximately 150 minutes to a root mean square error (RMSE) on the energy and forces of 0.9 meV and 23.9 meV/Å, respectively.

Comparison of the universal and specific machine learning potentials

The MACE-MP-0 is a machine learning potential using the MACE architecture that was trained on a parsed set of the materials project database¹⁶. The DFT energies were calculated with VASP¹⁷ using the PBE or PBE+U¹⁸ XC functional. MACE-MP-0 can reproduce qualitative trends for materials that are not included in the materials project database. MACE-MP-0 was used to equilibrate the generated structures before starting the active learning loop. All simulations were stable in MD simulations at 300 K and 0.1 MPa. To test the validity of MACE-MP-0, every MD simulation was performed with the MLP trained via Psiflow and MACE-MP-0.

The results obtained with the Psiflow MLP were very similar to the results obtained with MACE-MP-0. The trends obtained from the substituted perovskite and RP phase simulations are the same. The only clear difference was observed for the MD simulation of the one-shift RP phases. All MD simulations of the one-shift RP phase with MACE-MP-0 are unstable, and the structures always end up in the two-shift RP phase structure. Moreover, for a larger number of substitutions, the MACE-MP-0 is more likely to deform than the Psiflow MLP. The DFT level of theory and the applied basis sets are not the same for the two MLPs, which could explain these differences.

References

- (1) Lobato, I.; Van Aert, S.; Verbeeck, J. Progress and New Advances in Simulating Electron Microscopy Datasets Using MULTEM. *Ultramicroscopy* **2016**, 168, 17–27.
- (2) Verstraelen, T.; Vanduyfhuys, L.; Vandenbrande, S.; Rogge, S. Yaff, yet Another Force Field. http://molmod.ugent.be/software/. (accessed 2024-12-23)
- (3) Bussi, G.; Parrinello, M. Accurate Sampling Using Langevin Dynamics. *Phys. Rev. E* **2007**, 75 (5), 056707.
- (4) Feller, S. E.; Zhang, Y.; Pastor, R. W.; Brooks, B. R. Constant Pressure Molecular Dynamics Simulation: The Langevin Piston Method. *J. Chem. Phys.* **1995**, 103 (11), 4613–4621.

- (5) Vandenhaute, S.; Cools-Ceuppens, M.; DeKeyser, S.; Verstraelen, T.; Van Speybroeck, V. Machine Learning Potentials for Metal-Organic Frameworks Using an Incremental Learning Approach. NPJ Comput. Mater. 2023, 9 (1), 1–8.
- (6) Batatia, I.; Benner, P.; Chiang, Y.; Elena, A. M.; Kovács, D. P.; Riebesell, J.; Advincula, X. R.; Asta, M.; Baldwin, W. J.; Bernstein, N.; Bhowmik, A.; Blau, S. M.; Cărare, V.; Darby, J. P.; De, S.; Della Pia, F.; Deringer, V. L.; Elijošius, R.; El-Machachi, Z.; Fako, E.; Ferrari, A. C.; Genreith-Schriever, A.; George, J.; Goodall, R. E. A.; Grey, C. P.; Han, S.; Handley, W.; Heenen, H. H.; Hermansson, K.; Holm, C.; Jaafar, J.; Hofmann, S.; Jakob, K. S.; Jung, H.; Kapil, V.; Kaplan, A. D.; Karimitari, N.; Kroupa, N.; Kullgren, J.; Kuner, M. C.; Kuryla, D.; Liepuoniute, G.; Margraf, J. T.; Magdău, I.-B.; Michaelides, A.; Moore, J. H.; Naik, A. A.; Niblett, S. P.; Norwood, S. W.; O'Neill, N.; Ortner, C.; Persson, K. A.; Reuter, K.; Rosen, A. S.; Schaaf, L. L.; Schran, C.; Sivonxay, E.; Stenczel, T. K.; Svahn, V.; Sutton, C.; van der Oord, C.; Varga-Umbrich, E.; Vegge, T.; Vondrák, M.; Wang, Y.; Witt, W. C.; Zills, F.; Csányi, G. A Foundation Model for Atomistic Materials Chemistry. arXiv [physics.chem-ph], March 1, 2024, arXiv:2401.00096.
- (7) Grimme, S.; Antony, J.; Ehrlich, S.; Krieg, H. A Consistent and Accurate Ab Initio Parametrization of Density Functional Dispersion Correction (DFT-D) for the 94 Elements H-Pu. *J. Chem. Phys.* **2010**, 132 (15).
- (8) Perdew, J. P.; Burke, K.; Ernzerhof, M. Generalized Gradient Approximation Made Simple. *Phys. Rev. Lett.* **1996**, 77 (18), 3865.
- (9) Hutter, J.; Iannuzzi, M.; Schiffmann, F.; Vandevondele, J. Cp2k: Atomistic Simulations of Condensed Matter Systems. *Wiley Interdiscip. Rev. Comput. Mol. Sci.* **2014**, 4 (1), 15–25.
- (10) Goedecker, S.; Teter, M. Separable Dual-Space Gaussian Pseudopotentials. *Phys Rev B* **1996**, 54 (3), 1703.
- (11) VandeVondele, J.; Hutter, J. Gaussian Basis Sets for Accurate Calculations on Molecular Systems in Gas and Condensed Phases. *J. Chem. Phys.* **2007**, 127 (11).
- (12) Batatia, I.; Kovács, D. P.; Simm, G. N. C.; Ortner, C.; Csányi, G. M. MACE: Higher-Order Equivariant Message Passing Neural Networks for Fast and Accurate Force Fields. arXiv [stat.ML], January 26, **2023**, arXiv:2206.07697.
- (13) Vandenhaute, S.; Rogge, S. M. J.; Van Speybroeck, V. Large-Scale Molecular Dynamics Simulations Reveal New Insights into the Phase Transition Mechanisms in MIL-53(Al). *Front. Chem.* **2021**, 9, 7189203

- (14) Zhang, Z.; Liu, X.; Yan, K.; Tuckerman, M. E.; Liu, J. Unified Efficient Thermostat Scheme for the Canonical Ensemble with Holonomic or Isokinetic Constraints via Molecular Dynamics. *J. Phys. Chem. A* **2019**, 123 (28), 6056–6079.
- (15) Eastman, P.; Galvelis, R.; Peláez, R. P.; Abreu, C. R. A.; Farr, S. E.; Gallicchio, E.; Gorenko, A.; Henry, M. M.; Hu, F.; Huang, J.; Krämer, A.; Michel, J.; Mitchell, J. A.; Pande, V. S.; Rodrigues, J. P.; Rodriguez-Guerra, J.; Simmonett, A. C.; Singh, S.; Swails, J.; Turner, P.; Wang, Y.; Zhang, I.; Chodera, J. D.; De Fabritiis, G.; Markland, T. E. OpenMM 8: Molecular Dynamics Simulation with Machine Learning Potentials. *J. Phys. Chem. B* **2024**, 128 (1), 109–116.
- (16) Jain, A.; Ong, S. P.; Hautier, G.; Chen, W.; Richards, W. D.; Aguey-Zinsou, K. F.; Cholia, S.; Wolverton, C.; Agrawal, A.; Choudhary, A.; Persson, K. A. The Materials Project: A Materials Genome Approach to Accelerating Materials Innovation. *APL Mater.* **2013**, 1 (1), 011002.
- (17) Kresse, G.; Furthmüller, J. Efficient Iterative Schemes for Ab Initio Total-Energy Calculations Using a Plane-Wave Basis Set. *Phys. Rev. B* **1996**, 54 (16), 11169–11186.
- (18) Anisimov, V. I.; Zaanen, J.; Andersen, O. K. Band Theory and Mott Insulators: Hubbard U Instead of Stoner I. *Phys. Rev. B* **1991**, 44 (3), 943–954.